

Simulating Hydrodynamics in Cosmology with CRK-HACC

NICHOLAS FRONTIERE,^{1,2} J.D. EMBERSON,¹ MICHAEL BUEHLMANN,² JOSEPH ADAMO,^{2,3} SALMAN HABIB,^{1,2}
KATRIN HEITMANN,² AND CLAUDE-ANDRÉ FAUCHER-GIGUÈRE⁴

¹*CPS Division, Argonne National Laboratory, Lemont, IL 60439, USA*

²*HEP Division, Argonne National Laboratory, Lemont, IL 60439, USA*

³*Department of Astronomy and Steward Observatory, University of Arizona, Tucson, AZ 85721, USA*

⁴*Department of Physics and Astronomy and Center for Interdisciplinary Exploration and Research in Astrophysics (CIERA), Northwestern University, Evanston, IL 60201, USA*

ABSTRACT

We introduce CRK-HACC, an extension of the Hardware/Hybrid Accelerated Cosmology Code (HACC), to resolve gas hydrodynamics in large-scale structure formation simulations of the universe. The new framework couples the HACC gravitational N-body solver with a modern smoothed particle hydrodynamics (SPH) approach called CRKSPH. Conservative Reproducing Kernel SPH utilizes smoothing functions that exactly interpolate linear fields while manifestly preserving conservation laws (momentum, mass, and energy). The CRKSPH method has been incorporated to accurately model baryonic effects in cosmology simulations – an important addition targeting the generation of precise synthetic sky predictions for upcoming observational surveys. CRK-HACC inherits the performance design specifications of HACC and is optimized to run effectively on modern GPU-accelerated supercomputers. In this work, we summarize the primary solver components and present a number of standard validation tests to demonstrate efficacy, including idealized hydrodynamic and cosmological setups, as well as self-similarity measurements.

Keywords: methods: numerical – cosmology: theory – hydrodynamics

1. INTRODUCTION

Numerical simulations play a vital role in precision cosmology by providing accurate theoretical predictions of structure formation in the universe. Mock realizations explore the nature of dark matter and dark energy, probe the origins of primordial fluctuations, and facilitate new ways of investigating fundamental physics, such as the imposition of cosmological limits on the neutrino mass sum. Importantly, simulations can produce realistic synthetic measurements to help solve the (statistical) inverse problem of determining cosmological parameters – providing constraints on the Λ CDM model – and to categorize astrophysical and experimental systematics, crucial for the planning, calibration, and validation of observational surveys.

Traditionally, gravity-only N-body simulations have been the primary means to generate mock sky catalogs, attributable to their efficient computational cost and lack of model uncertainties (Angulo & Hahn 2021

provide an excellent overview of state-of-the-art simulation methods and challenges). The Hardware/Hybrid Accelerated Cosmology Code (HACC) was developed to performantly run gravity-only simulations on all modern supercomputing platforms, scaling to millions of cores and exploiting heterogeneous hardware such as GPUs (Habib et al. 2016 hereafter H16). However, accurate treatment of baryonic gas and its interplay with dark matter physics has become increasingly important for cosmological predictions, owing to the precise measurements of current and upcoming observational surveys that are sensitive to these effects (e.g., van Daalen et al. 2011; Harnois-Déraps et al. 2015; Copeland et al. 2018).

The field of hydrodynamic astrophysics simulations is rich, and significant progress has been made over the last few decades relating to the modeling of galaxy formation (see Naab & Ostriker 2017 and Vogelsberger et al. 2020 for recent reviews). In this paper, we study an extension of the HACC framework to include baryonic effects by incorporating a conservative reproducing kernel smoothed particle hydrodynamics (CRKSPH) solver described in Frontiere, Raskin, & Owen (2017) (henceforth abbrev-

viated as FRO17). The combined framework, called CRK-HACC, was developed to maintain all performance design characteristics of HACC, while improving its predictive capabilities.

Smoothed particle hydrodynamics (SPH) methods have a long history since the pioneering work of Lucy (1977) and Gingold & Monaghan (1977), and have become a staple Lagrangian-based approach in astrophysics codes (Rosswog 2009; Springel 2010b; Price 2012). Precise enforcement of conservation laws, Galilean invariance, trivial parallelization, and refinement that is inherently adaptive (where particles naturally evolve to high density regions), are some of the many advantages of SPH codes.

As described in detail in FRO17, CRKSPH was developed to leverage the benefits of SPH, while actively addressing several of its main difficulties, including the inability to exactly reproduce zeroth-order fields, and overly aggressive artificial viscosity models. Recently, there have been further extensions to incorporate radiation transport discretizations as well (Bassett & Owen 2021). This study is devoted to the application of CRKSPH in a cosmology framework, capitalizing on the accuracy of the solver, and serving as a basis for future work modeling numerous baryonic probes – such as Sunyaev-Zel’dovich maps, gravitational weak lensing measurements, gas-evolved synthetic sky catalogs, and the Lyman- α forest, to name a few. The *Borg Cube* simulation, described in Emberson et al. (2019), was the first application of the CRK-HACC solver utilized in this manner, specifically in a non-radiative setting.

The paper is organized as follows. In Section 2, we provide background information on the cosmological fluid equations, as well as a summary of the CRKSPH approach. Section 3 details all the primary modifications and additions to the HACC framework required in CRK-HACC. To confirm solver correctness, we present a series of validation experiments for idealized hydrodynamic and self-gravitating tests in Section 4. Furthermore, we measure self-similar scaling relations for scale-free initial condition cosmology simulations in Section 5. Finally, we conclude with a summary and discussion of future work in Section 6.

2. BACKGROUND EQUATIONS

We begin our discussion with an overview of both the expanding universe cosmology equations (Section 2.1), and the methodology behind the hydrodynamic CRKSPH solver (Section 2.2). Unless otherwise specified, we denote the comoving spatial coordinate as \mathbf{x} , where $\mathbf{r} = a(t)\mathbf{x}$ is the proper position, and $a(t)$ is the cosmic scale factor.

2.1. Cosmology Equations

The set of equations for an ideal fluid in an expanding Friedmann-Robertson-Walker (FRW) universe can be written in comoving units (Peebles 1980) as follows:

$$\frac{d\rho}{dt} = -\frac{1}{a^2}\rho\nabla\cdot\mathbf{p}, \quad (1)$$

$$\frac{d\mathbf{p}}{dt} = -a^2\frac{\nabla P}{\rho} - \frac{\nabla\phi}{a}, \quad (2)$$

$$\frac{du}{dt} = -\frac{1}{a^2}\frac{P}{\rho}\nabla\cdot\mathbf{p} - \frac{\dot{a}}{a}(3(\gamma-1)+2)u. \quad (3)$$

The pressure P , density ρ , and thermal energy per unit mass u couple via the equation of state

$$P = (\gamma - 1)\rho u, \quad (4)$$

with adiabatic index γ (often set to the monatomic value $\gamma = 5/3$). In our notation, $\mathbf{p} \equiv a^2\dot{\mathbf{x}} = a\mathbf{v}$, where \mathbf{v} is the proper peculiar velocity. The scalar (comoving) potential ϕ satisfies the Poisson equation

$$\nabla^2\phi = 4\pi G[\rho(\mathbf{x}, t) - \rho_m(t)], \quad (5)$$

where the background matter density $\rho_m = \Omega_m\rho_c$, in a universe with critical density ρ_c and matter fraction Ω_m , including dark matter and baryons. The scalar potential is related to the proper gravitational potential (Φ) as

$$\phi = a\Phi + \frac{1}{2}a^2\ddot{a}x^2. \quad (6)$$

We remark that the fluid equations are written in Lagrangian form, using the convective (material) derivative

$$d/dt = \partial/\partial t + \dot{\mathbf{x}}\cdot\nabla. \quad (7)$$

Moreover, the spatial derivatives are measured with respect to \mathbf{x} , e.g., $\nabla \equiv \nabla_{\mathbf{x}}$.

As is common for numerical solvers, the evolution equations in CRK-HACC are evaluated in dimensionless (“tilde”) units via the following transformations

$$\begin{aligned} \tilde{\mathbf{x}} &\equiv \mathbf{x}/x_0, \quad \tilde{t} \equiv tH_0, \quad \tilde{\rho} \equiv \rho/\rho_m, \\ \tilde{G} &\equiv \frac{3}{2}\Omega_m\frac{1}{4\pi}, \quad \tilde{\phi} \equiv \phi/(x_0^2H_0^2), \end{aligned} \quad (8)$$

where x_0 is the particle-mesh grid spacing L/n_g , the ratio of the comoving domain length (in $h^{-1}\text{Mpc}$) and the number of grid cells in a single dimension. As described in Section 3.1, the CRK-HACC time integrator incorporates steps with equal spacing in units of the scale factor. We introduce the temporal variable

$$y \equiv a^\alpha, \quad (9)$$

where α is a constant and the differential operators are obtained using the chain rule,

$$\frac{d}{d\bar{t}} = \frac{d}{dy} \frac{dy}{d\bar{t}} = \frac{d}{dy} \alpha y \frac{H}{H_0}. \quad (10)$$

Our canonical choice of time units is defined by $\alpha = 1$.

2.2. CRKSPH Equations

SPH is a Lagrangian approach that discretizes gas into fluid parcels traveling with the flow velocity. Arbitrary fluid quantities $\psi(\mathbf{x})$ are generally evaluated using an integral interpolant

$$\psi(\mathbf{x}) = \int \psi(\mathbf{x}') W(\mathbf{x} - \mathbf{x}', h) d\mathbf{x}', \quad (11)$$

where $W(\mathbf{x}, h)$ is a kernel of compact support (finite non-zero extent) with characteristic radius parameterized by the smoothing length h . Common selections for W are spherically symmetric functions, including B-splines (Schoenberg 1969) and Wendland kernels (Wendland 1995). The CRK-HACC solver follows the recommendation of Dehnen & Aly (2012), and utilizes a 4th order (C^4) Wendland function:

$$W_{C^4}(\eta, h) = \frac{495}{32\pi h^3} (1 - \eta)^6 (1 + 6\eta + \frac{35}{3}\eta^2), \quad (12)$$

with $\eta \equiv |\mathbf{x}|/h$, and unit kernel extent ($W_{C^4} = 0$ for $\eta \geq 1$). In general, SPH kernels integrate to unity and are required to asymptotically approach a δ -function when $h \rightarrow 0$, where the interpolant equation becomes exactly reproducing in the continuum limit.

Eq. 11 can be written in a discretized form as a summation over particle interactions between neighbors within the kernel support, viz.

$$\psi_i = \sum_j \psi_j V_j W(|\mathbf{x}_i - \mathbf{x}_j|, h_i) = \sum_j \psi_j V_j W_{ij}, \quad (13)$$

with V_j denoting the volume associated with each particle. In CRK-HACC, we express the particle volume as the inverse of the SPH number density n_i , namely

$$V_i^{-1} = n_i = \sum_j W(|\mathbf{x}_i - \mathbf{x}_j|, h_i). \quad (14)$$

Other representations, such as Voronoi volumes (e.g., Heß & Springel 2010), can be utilized as a substitute definition.

CRKSPH improves the accuracy of SPH interpolation by utilizing reproducing kernels (RKs), which exactly interpolate polynomial fields of a specified order (e.g., Liu et al. 1995; Liu & Jun 1998). Specifically, we employ first-order RK functions, which are constructed from

SPH kernels as follows:

$$\mathcal{W}_{ij}^R = A_i(1 + \mathbf{B}_i \cdot \mathbf{x}_{ij}) W_{ij}, \quad (15)$$

$$\begin{aligned} \nabla \mathcal{W}_{ij}^R &= \nabla A_i(1 + \mathbf{B}_i \cdot \mathbf{x}_{ij}) W_{ij} \\ &+ A_i(\nabla \mathbf{B}_i \cdot \mathbf{x}_{ij} + \mathbf{B}_i) W_{ij} \\ &+ A_i(1 + \mathbf{B}_i \cdot \mathbf{x}_{ij}) \nabla W_{ij}, \end{aligned} \quad (16)$$

where $\mathbf{x}_{ij} \equiv \mathbf{x}_i - \mathbf{x}_j$. The scalar and vector coefficients (A, \mathbf{B}) are determined by enforcing the zeroth and first moments of \mathcal{W}_{ij}^R integrate to 1 and 0, respectively; i.e., $\int \mathcal{W}_{ij}^R = 1$ and $\int \mathbf{x}_{ij} \mathcal{W}_{ij}^R = 0$ (see Appendix A in FRO17 for a complete derivation). The resulting kernels exactly reproduce linear fields over the particle interpolants.

RK functions are in general no longer symmetric for arbitrary particle distributions. The spherical symmetry of traditional SPH kernels allows for a simple discretization of the fluid equations that exactly conserve energy and momentum (summarized in Monaghan 2005), a desirable feature of SPH. Care must be taken when utilizing RK interpolation to ensure that the system preserves the same invariants. Originally developed for the Moving Least-squares SPH (MLSPH) approach described in Dilts (1999), the following inviscid hydrodynamic evolution equations (written for an expanding universe) maintain exact momentum and energy conservation for non-symmetric kernels:

$$m_i \frac{d\mathbf{p}_i}{dt} = \sum_j \frac{a^2}{2} V_i V_j (P_i + P_j) (\nabla \mathcal{W}_{ji}^R - \nabla \mathcal{W}_{ij}^R), \quad (17)$$

$$m_i \frac{du_i}{dt} = \sum_j \frac{1}{2a^2} V_i V_j P_j \dot{\mathbf{x}}_{ji} \cdot (\nabla \mathcal{W}_{ji}^R - \nabla \mathcal{W}_{ij}^R), \quad (18)$$

where m_i is the mass of each particle and $\dot{\mathbf{x}}_{ji} \equiv \dot{\mathbf{x}}_j - \dot{\mathbf{x}}_i$. These differential relations for momentum and energy describe the discretization of the first (pressure) term in fluid Eqs. 2 and 3. We observe that for any interaction pair (i,j) in the summation, $m_i(\frac{d\mathbf{p}}{dt})_{i \rightarrow j} = -m_j(\frac{d\mathbf{p}}{dt})_{j \rightarrow i}$, obeying Newton's third law.

Although the differential energy listed in Eq. 18 is fully conservative and can be evolved in conjunction with the momentum update from Eq. 17, in practice CRKSPH utilizes the “compatible energy” formalism of Owen (2014) to evolve the internal energy, with modifications outlined in FRO17. The procedure enforces energy conservation for a given momentum change provided by Eq. 17, as opposed to independently evolving the internal energy separately. The compatible energy update demonstrates favorable behavior in a number of adiabatic tests where entropy invariance is important, and is the fiducial energy integration procedure used in CRK-HACC.

The compatible differencing of comoving energy Δu_i for a particle over a time step Δt is calculated as

$$\Delta u_i = \sum_j \Delta u_{ij} \Delta t + \frac{\dot{a}}{a} (3(\gamma - 1) + 2) u_i, \quad (19)$$

$$\Delta u_{ij} = \frac{f_{ij}}{2a^4} [\mathbf{p}_j + \mathbf{p}'_j - \mathbf{p}_i - \mathbf{p}'_i] \frac{d\mathbf{p}_{ij}}{dt}, \quad (20)$$

$$\Delta E_{ij} = m_i \Delta u_{ij} + m_j \Delta u_{ji}, \quad (21)$$

$$\mathbf{p}'_i = \mathbf{p}_i + \frac{d\mathbf{p}_i}{dt} \Delta t, \quad (22)$$

$$f_{ij} = \begin{cases} \frac{\min(s_i, s_j)}{s_i + s_j}, & (\Delta E_{ij} \geq 0, s_i \geq s_j) \text{ or} \\ & (\Delta E_{ij} < 0, s_i < s_j); \\ \frac{\max(s_i, s_j)}{s_i + s_j}, & (\Delta E_{ij} \geq 0, s_i < s_j) \text{ or} \\ & (\Delta E_{ij} < 0, s_i \geq s_j), \end{cases} \quad (23)$$

where $s \equiv P/\rho^\gamma$ is the specific entropy, and $\frac{d\mathbf{p}_{ij}}{dt}$ is the pair-wise acceleration described by Eq. 17 (using $\frac{d\mathbf{p}_i}{dt} \equiv \sum_j \frac{d\mathbf{p}_{ij}}{dt}$). The first term in Eq. 19 represents the energy change due to the hydrodynamic impulse of each neighbor interaction, while the second term accounts for the energy loss from expansion – discretizations of the first and second terms in Eq. 3. The derivation of Δu_{ij} (Eq. 20) follows identically to FRO17 (Eq. 61 in that work), requiring a simple transformation to comoving variables ($\mathbf{v} \rightarrow \dot{\mathbf{x}} = \mathbf{p}/a^2$, $\mathbf{a}_{ij} \rightarrow \frac{1}{a^2} \frac{d\mathbf{p}_{ij}}{dt}$). The partition function f_{ij} determines the amount of energy transferred between two nodes given their pair-wise momentum change over a given time step. Any definition of f_{ij} will uphold energy conservation as long as $f_{ij} + f_{ji} = 1$. The specific entropy form utilized in Eq. 23 results in a physically motivated energy balancing, where cooler nodes are heated or hotter nodes are cooled, depending on the sign of the change in work for the interaction (ΔE_{ij}).

The SPH evolution equations require the addition of artificial viscosity to properly capture shock hydrodynamics. The traditionally used pair-wise viscosity prescription of Monaghan & Gingold (1983) (henceforth MG83) encapsulates the bulk (linear) and Von Neumann-Richtmyer (quadratic) viscosity within a viscous pressure Q , defined in comoving units as:

$$Q_i = \rho_i (-C_l c_{s,i} \mu_i + C_q \mu_i^2), \quad (24)$$

$$\mu_i = \min(0, \frac{\hat{h}_i}{a} \frac{\mathbf{u}_{ij} \cdot \mathbf{x}_{ij}}{|\mathbf{x}_{ij}|^2 + \hat{h}_i^2 \epsilon^2}), \quad (25)$$

where $\mathbf{u}_{ij} \equiv \mathbf{u}_i - \mathbf{u}_j$ is the difference in the proper velocities ($\mathbf{u} \equiv \mathbf{v} + \dot{a}\mathbf{x}$) of interacting particles, $c_s \equiv \sqrt{\gamma P/\rho}$ is the sound speed, $\epsilon = 0.1$ is a small number to avoid division by zero, and (C_l, C_q) are the viscous linear and quadratic coefficients set to (2.0, 1.0) in CRKSPH. Using a normalized smoothing length $\hat{h}_i \equiv h_i/n_h$ confines the

spatial dissipation scale to be roughly the local inter-particle separation, where n_h is a resolution parameter specifying the effective number of particles per smoothing length ($n_h = 4$ in our results, see Section 3.6). The implementation of artificial viscosity is trivial within Eqs. 17 and 18 by replacing the pressure P with the combined total pressure $P + Q$.

While the viscosity treatment of MG83 is simple and conservative, it has been shown to be excessively diffusive in certain situations, leading to the development of a number of modifications over the years (e.g., Balsara 1995; Morris & Monaghan 1997; Cullen & Dehnen 2010; Read et al. 2010). The novel viscosity model described in FRO17 was motivated by the work of Christensen (1990) to develop a “limited” viscosity variation of MG83. The peculiar velocity gradient is accurately measured with reproducing kernels by

$$\nabla \mathbf{v}_i = - \sum_j V_j (\mathbf{v}_i - \mathbf{v}_j) \otimes \nabla \mathcal{W}_{ij}^R. \quad (26)$$

The gradient can be utilized to project the proper velocity to the peculiar midpoint of a particle interaction pair, viz.

$$\begin{aligned} \hat{\mathbf{v}}_i &\equiv \mathbf{v}_i - \frac{1}{2} \phi_{ij} \nabla \mathbf{v}_i \cdot \mathbf{x}_{ij}, \\ \hat{\mathbf{u}}_i &\equiv \hat{\mathbf{v}}_i + \dot{a} \mathbf{x}_i, \end{aligned} \quad (27)$$

where an additional “limiter function” ϕ is introduced to vary the extent of the projection ($\phi \in [0, 1]$). Once the limiter is specified, the implementation of the modified MG83 viscosity is trivial by simply replacing \mathbf{u}_{ij} in Eq. 25 with $\hat{\mathbf{u}}_{ij} \equiv \hat{\mathbf{u}}_i - \hat{\mathbf{u}}_j$. Fundamentally, for linear velocity flows, the pairwise difference vanishes, shutting off the viscosity in a regime where numerical dissipation is unnecessary and undesirable. We emphasize that the projection is restricted to the peculiar component of the particle velocity, and not applied to the Hubble expansion term ($\dot{a}\mathbf{x}$); otherwise, the total projection would evaluate to $\hat{\mathbf{u}}_{ij} = \hat{\mathbf{v}}_{ij} + (1 - \phi_{ij}) \dot{a} \mathbf{x}_{ij}$, which would erroneously remove the expansion component in limited ($\phi = 1$) flows.

The limiter described in FRO17 was constructed to exclusively project the velocity in smooth flows, while returning to the standard non-projected MG83 viscosity for non-linear interactions. Explicitly, a modified symmetric van Leer limiter (van Leer 1974; Toro 1989) applied to the ratio of the velocity gradients of an interaction pair was utilized:

$$\phi_{ij} = \phi_{VL} \times \phi_{ad}, \quad (28)$$

$$\phi_{VL} = \max \left[0, \min \left[1, \frac{4r_{ij}}{(1 + r_{ij})^2} \right] \right], \quad (29)$$

$$r_{ij} = \frac{\nabla \mathbf{v}_i \cdot \mathbf{x}_{ij} \cdot \mathbf{x}_{ij}}{\nabla \mathbf{v}_j \cdot \mathbf{x}_{ij} \cdot \mathbf{x}_{ij}}, \quad (30)$$

$$\phi_{ad} = \begin{cases} \exp\left\{-\left(\frac{\eta_{ij}-\eta_{\text{crit}}}{\eta_{\text{fold}}}\right)^2\right\}, & \eta_{ij} < \eta_{\text{crit}}; \\ 1, & \eta_{ij} \geq \eta_{\text{crit}}, \end{cases} \quad (31)$$

$$\eta_{ij} = \min(|\mathbf{x}_{ij}|/h_i, |\mathbf{x}_{ij}|/h_j), \quad (32)$$

where ϕ_{VL} is the standard van Leer limiter, and the adjustment function ϕ_{ad} exponentially suppresses the limiter if particles are driven closer together than physically plausible; specifically, in units of $\eta = \mathbf{x}/h$, we expect particles to be spatially separated on order of $1/n_h$. Accordingly, the adjustment parameters ($\eta_{\text{crit}}, \eta_{\text{fold}}$) are fiducially set to $(1/n_h, 0.2/n_h)$, ensuring that the limiter be exclusively suppressed on scales smaller than the inter-particle separation.

3. FRAMEWORK COMPONENTS

A complete description of the software features in HACC is listed in H16. Design elements, such as performant I/O, manual memory management, and portability strategies, have all been carried over to CRK-HACC. In this section, we outline the primary simulation components that are unique to, or modified in, the extended framework.

3.1. Time Integrator

The separable Hamiltonian for an ideal fluid described in Section 2.1 is

$$H = m \frac{\mathbf{p}^2}{2a^2} + U(\mathbf{x}, \rho) + m \frac{\phi}{a} + S, \quad (33)$$

where $U(\mathbf{x}, \rho)$ is the internal energy, and S represents arbitrary source terms from additional astrophysics models (see Section 3.7). The Hamiltonian can be split into gravitational $H_G = m \frac{\phi}{a}$ and hydrodynamic $H_H = H_H^K + H_H^T + H_H^S$ terms, where $H_H^K = m \frac{\mathbf{p}^2}{2a^2}$, $H_H^T = U(\mathbf{x}, \rho)$ and $H_H^S = S$ are the kinetic, thermal and source components, respectively. The gravitational Hamiltonian can be further decomposed into a sum of fast and slow changing potentials $\phi = \phi_F + \phi_S \rightarrow H_G = H_G^F + H_G^S$; as summarized in Sections 3.2 & 3.3, ϕ_S represents a long-range potential, which is calculated by solving the Poisson equation (Eq. 5) using a high-order spectral particle-mesh (PM) approach (Hockney & Eastwood 1988; H16), and ϕ_F is a local short-range potential, computed by a modified TreePM method (Barnes & Hut 1986; Gafton & Rosswog 2011).

For a general Hamiltonian system $H(z, t)$, with $z = (q, p)$ canonical coordinates, the equations of motion are expressed by $\dot{z} = \{z, H\}_P$, where $\{\cdot, \cdot\}_P$ is a Poisson bracket. The dynamic solution $z(t)$ is described

by the time evolution operator $\hat{U}(t) \equiv \exp(-t\{H, \cdot\}_P)$, where $z(t) = \hat{U}(t)z(0)$.

Let $\hat{U}_i(y)$ represent the time propagator for each individual Hamiltonian component of Eq. 33 (e.g., $\hat{U}_G(y) = \exp(-y\{H_G, \cdot\}_P)$), where the temporal variable y is specified in Eq. 9. The evolution operators can be expressed as discretized particle state updates over a given time step Δy (Quinn et al. 1997):

$$\hat{U}_G^S(\Delta y) : \mathbf{p}_i \mapsto \mathbf{p}_i - \frac{\nabla \phi_S}{a} \frac{dt}{dy} \Delta y, \quad (34)$$

$$\hat{U}_G^F(\Delta y) : \mathbf{p}_i \mapsto \mathbf{p}_i - \frac{\nabla \phi_F}{a} \frac{dt}{dy} \Delta y, \quad (35)$$

$$\hat{U}_H^T(\Delta y) : \begin{cases} \mathbf{p}_i \mapsto \mathbf{p}_i + \frac{d\mathbf{p}_i}{dt} \frac{dt}{dy} \Delta y, \\ u_i \mapsto u_i + \Delta u_i \frac{dt}{dy} \Delta y, \end{cases} \quad (36)$$

$$\hat{U}_H^K(\Delta y) : \mathbf{x}_i \mapsto \mathbf{x}_i + \frac{\mathbf{p}_i}{a^2} \frac{dt}{dy} \Delta y, \quad (37)$$

$$\hat{U}_H^S(\Delta y) : \begin{cases} \mathbf{p}_i \mapsto \mathbf{p}_i + S_p \frac{dt}{dy} \Delta y, \\ u_i \mapsto u_i + S_u \frac{dt}{dy} \Delta y, \\ \mathbf{x}_i \mapsto \mathbf{x}_i + S_x \frac{dt}{dy} \Delta y, \end{cases} \quad (38)$$

where we generally label the source terms S_p , S_u , and S_x to represent any model that affects the relevant state variable. The changes for momentum ($\frac{d\mathbf{p}_i}{dt}$) and energy (Δu_i) are taken from Eqs. 17 and 19, respectively. Note, the derivative $\frac{dy}{dt}$ (Eq. 10) is used to convert the time stepping variables to y -units.

We can construct a discretized time integrator $\hat{U}(\Delta y)$ by composing the evolution propagators as follows

$$\hat{U}_{\text{SR}}(\Delta y) = \hat{U}_G^F\left(\frac{\Delta y}{2}\right) \hat{U}_H(\Delta y) \hat{U}_G^S\left(\frac{\Delta y}{2}\right), \quad (39)$$

$$\hat{U}(\Delta y) = \hat{U}_G^S\left(\frac{\Delta y}{2}\right) \hat{U}_{\text{SR}}(\Delta y) \hat{U}_G^S\left(\frac{\Delta y}{2}\right), \quad (40)$$

where \hat{U}_{SR} encapsulates all of the “short-range” operators. In the case of a simple inviscid fluid (no artificial viscosity or sources), it can be shown that for a fixed time step Δy , the above integrator is second-order convergent, and is both symplectic (a volume-preserving phase space map) and time reversible (see, e.g., Yoshida 1990; Forest & Ruth 1990; Saha & Tremaine 1992).

Similarly, we can expand the hydrodynamic (\hat{U}_H) operator as

$$\hat{U}_V(\Delta y) = \hat{U}_H^T\left(\frac{\Delta y}{2}\right) \hat{U}_H^K(\Delta y) \hat{U}_H^T\left(\frac{\Delta y}{2}\right), \quad (41)$$

$$\hat{U}_H(\Delta y) = \hat{U}_V(\Delta y) \hat{U}_H^S(\Delta y). \quad (42)$$

In the absence of sources ($H_H^S = 0, \hat{U}_H^S = \mathbb{1}$), the fluid integrator becomes the commonly used second-order velocity Verlet operator ($\hat{U}_H = \hat{U}_V$), where our implemen-

tation is similar to Saitoh & Makino (2016):

$$\hat{U}_V(\Delta y) : \begin{cases} \mathbf{p}^{\frac{1}{2}} = \mathbf{p}^0 + \frac{1}{2} \frac{d\mathbf{p}}{dt}(\mathbf{x}^0, \mathbf{p}^0, u^0) \frac{dt}{dy} \Delta y, \\ u^{\frac{1}{2}} = u^0 + \frac{1}{2} \Delta u(\mathbf{x}^0, \mathbf{p}^0, u^0) \frac{dt}{dy} \Delta y, \\ \mathbf{x}^1 = \mathbf{x}^0 + \mathbf{p}^{\frac{1}{2}} \frac{1}{a^2} \frac{dt}{dy} \Delta y, \\ \mathbf{p}_p^1 = \mathbf{p}^{\frac{1}{2}} + \frac{1}{2} \frac{d\mathbf{p}}{dt}(\mathbf{x}^0, \mathbf{p}^0, u^0) \frac{dt}{dy} \Delta y, \\ u_p^1 = u^{\frac{1}{2}} + \frac{1}{2} \Delta u(\mathbf{x}^0, \mathbf{p}^0, u^0) \frac{dt}{dy} \Delta y, \\ \mathbf{p}^1 = \mathbf{p}^{\frac{1}{2}} + \frac{1}{2} \frac{d\mathbf{p}}{dt}(\mathbf{x}^1, \mathbf{p}_p^1, u_p^1) \frac{dt}{dy} \Delta y, \\ u^1 = u^{\frac{1}{2}} + \frac{1}{2} \Delta u(\mathbf{x}^1, \mathbf{p}_p^1, u_p^1) \frac{dt}{dy} \Delta y, \end{cases} \quad (43)$$

using \mathbf{p}_p^1 and u_p^1 as “predictive” momentum and energy at the end of a given step; when coupled to the gravity solver, the input velocities for the derivative calculation include predictions that account for the PM and short-range gravitational accelerations as well.

All sources are completely encapsulated by the \hat{U}_H^S operator in Eq. 42, which is composed with the Verlet integrator via first-order Strang splitting (Strang 1968). In future work, we will describe the inclusion of source terms to model the effects of galaxy formation physics.

Evaluating Eq. 40 using a global synchronized time stepper would require discretized intervals small enough to accurately resolve each operator for all particles. In reality, global stepping is computationally demanding and wasteful, as the dynamic time scales to properly integrate each particle can vary considerably. Given that the long-range gravity operator $\hat{U}_G^S(y)$ is slowly varying by definition, we can “subcycle” (Tuckerman et al. 1992; Duncan et al. 1998) the short-range operators as follows

$$\hat{U}(\Delta y) = \hat{U}_G^S\left(\frac{\Delta y}{2}\right) \underbrace{\left[\hat{U}_{\text{SR}}(\Delta y')\right]^m}_{\hat{U}_{\text{SR}}(\Delta y') \dots \hat{U}_{\text{SR}}(\Delta y')} \hat{U}_G^S\left(\frac{\Delta y}{2}\right), \quad (44)$$

where $\Delta y' = \Delta y/m$, for m -integer subcycles. Consistent with the HACC integrator, the PM step length Δy is selected to be evenly spaced in a , keeping the number of gravity subcycles fixed (typically $m = 4$) to maintain symplecticity.[†]

Following the integration approach of Saitoh & Makino (2010), the hydrodynamic operator is further subcycled into smaller steps $\Delta y'' = \Delta y'/n$ via the map

composition

$$\hat{U}_{\text{SR}}(\Delta y') = \hat{U}_G^F\left(\frac{\Delta y'}{2}\right) \underbrace{\left[\hat{U}_H(\Delta y'')\right]^n}_{\hat{U}_H(\Delta y'') \dots \hat{U}_H(\Delta y'')} \hat{U}_G^F\left(\frac{\Delta y'}{2}\right). \quad (45)$$

Unlike the gravity operators, which are synchronously applied to all particles, the hydrodynamic integration is performed hierarchically in power-of-two ($n = 2^l$) time bins, where the level l is calculated for each particle based on a combined Courant-Friedrichs-Lewy (CFL) and acceleration time-stepping criteria (e.g., Hernquist & Katz 1989; Springel 2005). Specifically, gas particles measure minimum time intervals $\Delta y_{\text{min},i}$ following

$$v_{\text{max},i} = \max(v_{\text{sig},i}, c_s, c_{sq}, \frac{\hat{h}_i}{a} |\nabla \cdot \mathbf{u}_i|), \quad (46)$$

$$\Delta y_{\text{hyd},i} = \frac{C_{\text{CFL}} \hat{h}_i}{v_{\text{max},i}} \frac{dy}{dt}, \quad (47)$$

$$\Delta y_{\text{acc},i} = \sqrt{\frac{\min(\hat{h}_i, r_{\text{soft}})}{|\mathbf{a}_{\text{tot}}|}} \frac{dy}{dt}, \quad (48)$$

$$\Delta y_{\text{min},i} = \min(\Delta y_{\text{hyd},i}, \Delta y_{\text{acc},i}), \quad (49)$$

to assign a time step level satisfying $\Delta y_{\text{min},i} > \Delta y'/2^l$. The Courant condition $\Delta y_{\text{hyd},i}$ employs a CFL coefficient $C_{\text{CFL}} = 0.25$, normalized smoothing length \hat{h}_i (as in Eq. 25), maximum viscous sound speed $c_{sq} = \sqrt{\zeta Q_i / \rho_i}$ (Eq. 24 and $\zeta = 4$), velocity divergence magnitude $|\nabla \cdot \mathbf{u}_i| = |\text{Tr } \nabla \mathbf{v}_i + 3\dot{a}|$ (using the trace of Eq. 26), and maximum neighbor signal velocity $v_{\text{sig},i} = \max_j v_{\text{sig},ij}$ with

$$v_{\text{sig},ij} = \min \left(\frac{(\dot{\mathbf{x}}_{ij} + \frac{\dot{a}}{a} \mathbf{x}_{ij}) \cdot \mathbf{x}_{ij}}{|\mathbf{x}_{ij}|}, 0.0 \right). \quad (50)$$

The acceleration criteria $\Delta y_{\text{acc},i}$ is taken from Durier & Dalla Vecchia (2011), using the combined hydrodynamic and gravity particle (peculiar) acceleration $\mathbf{a}_{\text{tot}} = \frac{1}{a^2} \left(\frac{d\mathbf{p}_i}{dt} - \frac{\nabla \phi}{a} \right)$ (from Eqs. 2 and 17), and simulation parameter r_{soft} denoting the gravitational softening length.

As described in Section 3.3, the short-range force solvers use a tree method, where the number of particles per leaf is roughly a few hundred. For time stepping, individual particles measure the minimum $\Delta y_{\text{min},\text{leaf}}$ required to resolve all elements in a leaf, which in turn determines a leaf-level l_{leaf} . Consequently, the leaves themselves are hierarchically time step-binned as opposed to individual particles. Following Durier & Dalla Vecchia (2011), leaves can move to smaller time bins as required, but can only jump to shallower levels every other time step. Furthermore, we utilize a time stepping limiter as

[†] Without uniform gravity subcycling, conservation of momentum is lost in addition to symplecticity. Recovering the former can be achieved using second-order hierarchical Hamiltonian splitting (Pelupessy et al. 2012; Zhu 2021; Springel et al. 2021).

described in Saitoh & Makino (2009); consistent with that work, we enforce the placement of all neighboring interacting leaves in bins that are within $f_l = 2$ time step levels of each other ($l_{\text{leaf},i} \leq f_l l_{\text{leaf},j}$), found to be a necessary condition for accurate propagation of shock waves using hierarchical time stepping. Without a limiter, the level of a neighboring leaf may be too shallow to properly resolve a high-velocity signal, a problem that would not be encountered with global time stepping. The CRK-HACC limiter is technically more conservative than Saitoh & Makino (2009), as it is enforced for leaves as opposed to individual particles (see Section 4.1.2 for a demonstration of the limiter accuracy on the Sedov-Taylor blast wave).

To summarize, at every PM step (length Δy), all particles apply the slowly varying long-range gravity operator \hat{U}_G^S . Each particle then evaluates the short-range propagator \hat{U}_G^F over a smaller gravity-subcycle $\Delta y'$. Particle leaves are further integrated using hydro-subcycles $\hat{U}_H(\Delta y'')$ that can vary in length (level) depending on the dynamics of each particle, and are limited to ensure neighboring leaves are within two levels. In practice, all particles are integrated at the smallest hydro interval, where each particle position is updated using the “drift” operator \hat{U}_H^K ; at every hierarchical subcycle, all (“active”) gas leaves that require force updates will evaluate the necessary derivatives and update their state-variables (following Eq. 42), while the remaining (“passive”) leaves are simply streamed.[†] At the conclusion of the hydro subcycles, the next gravity subcycle operator is applied, and the process repeats until the entire PM step interval has been integrated.

3.2. Gravitational Spectral Solver

The long-range (LR) gravity force operator in CRK-HACC is lifted from the HACC framework described in H16. Each species is mass deposited on a grid using Cloud-in-Cell (CIC) interpolation. The Poisson equation (Eq. 5) is solved with a spectral method that employs a Gauss-sinc k -space filter, a fourth-order Super-Lanczos spectral differentiator (Hamming 1998), and a sixth-order Green’s function. This approach provides a well-behaved decomposition of the gravitation potential into a long-range contribution from the PM solver, and

a short-range component at a fixed handover scale r_s (typically set to a few grid units).

The LR force calculation is MPI communication dominant, requiring an efficient and scalable Fast Fourier Transform (FFT). The HACC FFT package called SWFFT is publicly available,^{††} and uses a 3D “pencil” data decomposition for scalability. SWFFT has run effectively on millions of MPI ranks and is a key component of the HACC performance design strategy. As described in Section 3.1, the LR gravity operator is slowly varying, allowing for subcycling of computationally demanding short-range solvers that are node-local and do not require MPI communication. Thus, HACC and, by extension CRK-HACC, achieve ideal scaling using the portable spectral solver, while modularizing the short-range kernels to small code segments that are individually optimized (and potentially rewritten in domain specific languages such as CUDA) for the targeted hardware of a given machine.

3.3. Short-range Force Solvers

The CRK-HACC short-range gravitational force operator is similar to the “TreePM” solver in HACC. Particles are sorted into 3D chaining mesh (CM) bins (Hockney & Eastwood 1988) of side-length equal to the force handover scale r_s , whereby elements in each cell need only interact with themselves and neighboring bins. In parallel, each cell is further decomposed using a recursive coordinate bisection (RCB) tree (Gafton & Rossowog 2011), where leaves are recursively subdivided into two groups using a division line passing through the center of mass of a given enclosing leaf; the division line is drawn perpendicular to the longest side of each partition. The base leaves contain roughly N_{ppl} particles, where $N_{ppl} \in [128, 256]$ is typically optimal on GPU hardware. For efficiency, the tree construction is only performed once per gravitation PM step, where leaf metadata (bounding box information) is updated at the smallest time steps when particles are streamed. This means that the volume partitioning of leaves will overlap over the course of a PM step, and chaining mesh domains will become “fuzzy.”

An important modification in CRK-HACC is the indexing of the leaves. As opposed to storing the full tree hierarchy, only the base leaves are kept in a flattened contiguous data structure. Retaining the entire tree allows for efficient interaction calculations that can exploit multipole approximations of parent leaves, where leaf pairs that do not satisfy an opening angle criterion

[†] A note on streaming passive particles: instead of using the \hat{U}_H^K map $\mathbf{x}_i \mapsto \mathbf{x}_i + \frac{\mathbf{p}_i}{a^2} \frac{dt}{dy} \Delta y$, which simulates linear trajectories with constant velocity – we use a correction to integrate parabolic trajectories via $\mathbf{x}_i \mapsto \mathbf{x}_i + \frac{\mathbf{p}_i}{a^2} \frac{dt}{dy} \Delta y + \frac{1}{2} \frac{d\mathbf{p}_i}{dt} \frac{dt}{dy} (\Delta y)^2$ with constant acceleration. The correction results in the same total drift at the end of an active step, but allows for a more accurate integration at the smaller time intervals where the particle is passive.

^{††} <https://xgitlab.cels.anl.gov/hacc/SWFFT>

can interact with their monopole/quadrupole moments without requiring deeper traversals (see, e.g., Gafton & Rosswog 2011; Springel et al. 2021). While this approach is optimal on a CPU, traversing a tree data structure can be difficult on GPUs, which prefer contiguous simple data accesses. We, therefore, exploit the locality of the CM data structure, which already restricts all leaf communication to cell neighbors, and assemble interaction lists by processing the metadata of all base leaves in a given cell neighborhood. Moreover, since the leaves are relatively fat (as N_{ppl} is large), multipole interactions of base leaves can still significantly improve efficiency by not requiring as many direct N^2 leaf interactions.

The CRK-HACC hydrodynamic force solver utilizes the same tree data structure described above for gravity. The leaf metadata includes a baryon interaction domain, calculated by extending the bounding box to enclose the maximal smoothing length of the particles within the leaf. At every hydro subcycle, each active leaf assembles all interaction leaf pairs by visiting neighboring CM cells within the designated interaction distance. Again, as the data structure is contiguous, this operation is optimal on GPUs. Moreover, all hydro operators utilize the same interaction list, which need only be assembled once per hydro subcycle, and reused for each kernel.

3.4. Particle Overloading

A typical 3D domain decomposition in cosmology simulations assigns cuboid MPI rank (node) volumes with edge extents ranging from $32 - 500 h^{-1}\text{Mpc}$. Particles within each local partition are “alive”, and evolved following the integration approach detailed in Section 3.1. To reduce neighboring communication between nodes required to resolve boundaries, CRK-HACC employs a particle overloading approach discussed in H16. Each node extends its local boundary by an “overload” length (commonly $2 - 10 h^{-1}\text{Mpc}$), where tracers are replicated from the overlapping domains of neighboring ranks, and marked as “ghost” particles. The overload regions are analogous to ghost zones in grid codes, where in our case the alive particles are accurately updated using the ghost copies.

During each PM step, particles are CIC interpolated to a grid, where the gravitational spectral solver (Section 3.2) calculates the long-range potential. For each of the smaller subcycles (both gravitational and hydrodynamic), elements in the alive node regions accurately calculate the short-range forces using a combination of the alive and ghost particle sets, without the need for communication from other ranks. The ghost particles are similarly updated, with the exception that

particles near the extended domain edge do not update their local forces; specifically, particles within the gravitational handover length r_s of the domain boundary are only streamed, to avoid significant errors due to the anisotropic distribution at the edges. Nevertheless, in baryonic simulations, we still update the geometric properties (volume and density) of edge particles, particularly if they interact with alive neighbors.

The overload lengths are selected to be large enough, such that the integration errors incurred at the boundary do not “leak” into the alive regions. Periodically, ghost particles are “refreshed”, where the existing replications are removed and replaced by updated alive particles from neighboring ranks. In CRK-HACC this is done every PM step to be conservative and memory efficient, however this can be extended to longer time intervals with appropriately enlarged overload lengths.

We emphasize how the overloading procedure designed originally for the gravity forces in HACC is appropriate for CRK-HACC, which has the inclusion of hydrodynamic interactions. Unlike the short-range gravity force, which is restricted to a finite interaction radius r_s , hydrodynamic forces use an approximately fixed neighbor extent and can therefore include longer spatial interactions. However, in the default configuration of cosmology simulations, r_s is roughly the same as the smoothing length for a particle distribution of overdensity $\delta \sim 1$, and consequently, in clustered regimes the hydro forces are much smaller in extent than the gravitational length scales. As a result, the error leakages from the boundaries are typically much smaller for the hydro forces in dense distributions. In void regions ($\delta \ll 1$), smoothing lengths can grow very large, where naively requiring encompassing overload lengths would be highly memory inefficient. Conveniently, we have found that using the standard gravity-informed overload extents incur negligible errors in baryon simulations, as the void regions are already heavily undersampled, where relaxing resolution fidelity is in fact inconsequential.

We conclude with two remarks about overloading. Firstly, the procedure is extensible to the inclusion of astrophysical subgrid sources (summarized in Section 3.7), where attention to feedback model extent and stochastic processes is required; we leave the discussion of the particular nuances involved in these models to a future communication. Secondly, in GPU-accelerated systems, device memory is commonly imbalanced compared to host RAM. In response, we further decompose local node extents into smaller (similarly overloaded) subvolumes that can be independently transferred and evolved on a GPU over a full PM step. This procedure has the additional benefit that the smaller domains can be op-

tionally load-balanced across the machine, which can be particularly beneficial when simulations evolve into highly imbalanced low-redshift clustered regimes; this approach was first discussed in H16 (Section 3.3 in that work), and has been incorporated into CRK-HACC.

3.5. Cosmological Initial Conditions

As described in Heitmann et al. (2010), the HACC initial conditions (IC) generator distorts a grid arrangement of particles using the Zel’dovich approximation (Zel’dovich 1970); a random white noise generator[†] is convolved with a total matter transfer function (provided by e.g. CAMB Lewis et al. 2000 or CLASS Blas et al. 2011) and is subsequently mapped to a displacement field. The initial velocities in such an approach are proportional to the displacement, obviating the need for velocity transfer functions.

The CRK-HACC multi-species extension of the IC generator allows for the flexibility to initialize both grid and glass particle distributions. In the latter case, we construct the glass by evolving a random particle distribution in an Einstein–de Sitter universe with repulsive gravity until a quasi-equilibrium state is reached (White 1994). As the resulting particle configuration is pseudo-random, we perform an inverse CIC interpolation from the displacement field to the glass positions, where we minimize the interpolation error by convolving the white noise field with a spectral sinc filter (Hockney & Eastwood 1988).

For multi-species grid initial conditions, we lay a secondary lattice for gas particles, generally offset by a distance Δ from the dark matter arrangement. To avoid the necessity of interpolation to the baryon locations, we apply the Fourier phase shift $e^{-ik\Delta}$ to the white noise field. This procedure circumvents the necessity to calculate displacements for both species on a larger grid with, e.g., $2 \times N^3$ elements in the case $\Delta = 1/2$ in grid units (e.g., Valkenburg & Villaescusa-Navarro 2017).

Multi-species ICs, in particular, come with further challenges. For example, it is a common approach in cosmological hydrodynamic simulations to initialize both the dark matter and baryons using the total matter transfer function (as described above). However, this is technically incorrect as the two species have noticeably distinct transfer functions at typical initialization redshifts owing to evolutionary differences in the early universe (e.g., Angulo et al. 2013). Consequently, we

have added the capability to generate dark matter and baryons distributions with their respective density and velocity transfer functions. Different studies (e.g., Angulo et al. 2013; Bird et al. 2020; Hahn et al. 2021) have reported that this approach can introduce large-scale biases in the growth of each species when the force resolution is finer than the mean inter-particle separation. We have found the same behavior in CRK-HACC and plan to investigate accordingly in upcoming work.

There are a number of additional complexities in both gravity-only and multi-species initial conditions that should be stated. Firstly, the initial displacements and velocities must be sufficiently precise, a quality dependent on the order of perturbation theory and the initial redshift z_{in} . Moreover, consideration of the force solver accuracy when the displacements are small is necessary, as well as avoidance of nonphysical grid-imprinting, both of which are again conditional on z_{in} . We refer the reader to, e.g., Lukić et al. (2007); Heitmann et al. (2010); L’Huillier et al. (2014) as references, noting that we intend to explore these effects using CRK-HACC more thoroughly as well.

3.6. Kernel Selection and Smoothing Length

At a given resolution, the choice of smoothing kernel $W(\mathbf{x}, h)$ has been shown to be arbitrary in CRKSPH (see Appendix D of FRO17). Since the RK corrections specified in Eqs. 15 and 16 will modify a general SPH kernel function to be first-order consistent, it is unsurprising that the particular selection of interpolant is largely inconsequential. As described in Section 2.2, CRK-HACC utilizes the C^4 Wendland Kernel (Eq. 12). This selection was made to avoid the piece-wise functional definition of B-splines (particularly ill-suited for GPUs), in addition to being the “optimal” SPH kernel for simulations with $N \sim 200$ particle neighbors (as studied in Dehnen & Aly 2012). The standard resolution choice in CRK-HACC is for the smoothing length to radially enclose 4 particles ($n_h = 4$, for C^4), corresponding to approximately $N_{res} = 268$ neighbors.

The particle smoothing length h_i is related to the total number of neighbors by

$$N_i = \frac{4}{3}\pi h_i^3 n_i = \frac{4}{3}\pi h_i^3 \sum_j W(|\mathbf{x}_i - \mathbf{x}_j|, h_i), \quad (51)$$

with n_i approximating the particle number density using an SPH summation (see Eq. 14). This equation is commonly solved iteratively (e.g., Cullen & Dehnen 2010; Hopkins 2015) to determine h_i given a target resolution $N_i = N_{res}$. While convergence of the root-finding can be fast, on a GPU it is programmatically simpler to evolve h_i over time than to implicitly determine it.

[†] We use the Threefry counter-based pseudorandom number generator described in Salmon et al. (2011), which has the benefit of being highly efficient and parallelizable while also producing machine-independent random numbers.

To ensure a well-behaved solution for the evolved smoothing length, we follow the approach of [Thacker et al. \(2000\)](#). On a given time step, we measure the current neighbor count N_i from Eq. 51. The smoothing length is then adjusted following

$$\tilde{h}_i = h_i(1 - \lambda + \lambda\Delta_N), \quad (52)$$

where λ is a weighting coefficient, and $\Delta_N^3 \equiv (N_{res}/N_i)$ is the ratio of the target and measured neighbor counts. If $\Delta_N = 1$, $\tilde{h}_i = h_i$ by construction, leaving the smoothing length unaltered. The weighting function is given by

$$\lambda = \begin{cases} 0.2(1 + \Delta_N^2), & \Delta_N < 1; \\ 0.2(1 + 1/\Delta_N^3), & \Delta_N \geq 1. \end{cases} \quad (53)$$

We have confirmed that the evolved smoothing length procedure produces similarly accurate solutions compared to iterative solvers for the relevant hydrodynamic and cosmological problems studied using CRK-HACC.

3.7. Additional Physics

Sub-resolution (“subgrid”) models are necessary to emulate astrophysical processes – such as those involved in galaxy formation – that occur at scales smaller than the resolution limit of a simulation. A detailed investigation of the validation and calibration of subgrid models is beyond the scope of this paper, where we restrict our focus to non-radiative simulations. However, we will briefly summarize the additional physics options currently implemented within CRK-HACC for completeness.

The framework includes a radiative cooling and heating model that assumes gas to be optically thin and present in a spatially uniform time-varying ultraviolet background taken from either [Haardt & Madau \(2012\)](#) or [Faucher-Giguère \(2020\)](#). Similar to [Wiersma et al. \(2009\)](#), the cooling rates are calculated using the simulation code CLOUDY,[†] which further accounts for the inclusion of metals, combined with inverse Compton cooling from the cosmic microwave background (CMB). In practice, metal-line cooling is calculated from the total gas metallicity, as opposed to tracking element-by-element contributions. This simplification is justified because we will not resolve the necessary scales to properly model individual chemical yields, in addition to element corrections marginally affecting the overall photoionization model, particularly on cosmological scales (see, e.g., [Wiersma et al. 2009](#)). For a given UV back-

ground model, we use CLOUDY to produce a complete cooling rate table in four dimensions – metallicity, density, temperature, and helium abundance for a range of redshifts. The cooling function for each particle is interpolated from this table, where the evolved energy is calculated using the exact integration technique of [Townsend \(2009\)](#).

Star formation and supernova feedback are treated using the hybrid multi-phase model described in [Springel & Hernquist \(2003\)](#); above a specified density threshold, interstellar medium (ISM) gas is evolved via an effective equation of state, where stars form stochastically. Additionally, galactic outflow (wind) models are incorporated to quench star formation. The generated winds are likewise stochastic and scale with the star formation rate, following similarly to the work presented in [Vogelsberger et al. \(2014\)](#) and [Pillepich et al. \(2018\)](#). Lastly, star particles chemically enrich the ISM gas over time. This is achieved by integrating the average stellar enrichment rates from the FIRE simulations ([Hopkins et al. 2018](#)).

Finally, we have incorporated a selection of active galactic nuclei (AGN) models based on the standard prescriptions described in [Springel et al. \(2005\)](#); [Sijacki et al. \(2007\)](#); [Booth & Schaye \(2009\)](#); [Weinberger et al. \(2016\)](#). AGNs are represented by black hole “sink” particles that stochastically accrete nearby gas. The AGN mass grows proportionally to the Bondi-Hoyle-Lyttleton rate ([Bondi & Hoyle 1944](#); [Hoyle & Lyttleton 1939](#)), capped to never exceed the Eddington limit. Every halo above an assigned mass limit is seeded with a black hole, and proximate AGN particles are allowed to merge. AGN feedback is implemented using a combination of thermal and kinetic sources at a rate proportional to the mass accretion. In “quasar” or high accretion mode, black holes inject thermal energy to the surrounding gas. For “radio” low accretion black holes, kinetic energy is deposited stochastically on neighboring gas particles.

3.8. Analysis Capabilities

COSMOTOOLS is a software toolkit in HACC used for both in situ and post-processing analyses. Standard queries involve friends-of-friends (FOF, [Davis et al. 1985](#)) and spherical overdensity (SO, [Lacey & Cole 1994](#)) halo finding, including mass function and concentration measurements ([Child et al. 2018](#)), as well as the generation of detailed property and profile catalogs. HACC also includes tools for extracting particle light-cones, determining correlation functions and power spectra, merger tree construction, and halo “core” tracking (see, [Heitmann et al. 2021](#) and [Frontiere et al. 2021](#) for detailed descriptions of HACC outputs from recent state-of-the-art *Last Journey* and *Farpoint* simulations).

[†] <https://gitlab.nublado.org/cloudy/cloudy/-/wikis/home>

All analysis codes have been incorporated into CRK-HACC, where outputs are generated for each particle species when applicable – such as stellar, gas and dark matter power spectra, light cones, and halo profiles. Baryon-specific measurements, including computing galaxy catalogs (similar to Schaye et al. 2015), state variable (density, temperature, entropy) phase diagrams, global statistics (e.g., star formation rate density), and Lyman- α skewer tracings (following Lukić et al. 2014) have also been implemented. The tools have been developed for optimum performance on GPUs, where we utilize the publicly available ArborX software[†] (Lebrun-Grandié et al. 2020) for a selection of computationally demanding tasks, particularly halo/galaxy finding; for example, the GPU-accelerated FOF halo finder is over an order of magnitude faster than an equivalent CPU-optimized threaded algorithm. A detailed description of the CRK-HACC baryon analysis pipeline and GPU-performance optimization will be reported in a forthcoming paper.

4. STANDARD VALIDATION

With the framework components of CRK-HACC specified, we now present a range of conventional tests to evaluate the implementation of the new hydrodynamic solver. CRK-HACC utilizes compile-time options that can simulate fluids in a non-cosmological background using natural units. We individually validate the CRK-SPH integrator with traditional fluid experiments (Section 4.1), in addition to presenting results from gravitational collapse and standardized cosmological simulations (Section 4.2).

4.1. Pure Hydrodynamic Tests

Idealized fluid simulations are important to establish efficacy of the SPH solver. Here, we consider three standard hydrodynamic test problems: the *Sod shock tube*, *Sedov-Taylor blastwave*, and the *Kelvin-Helmholtz instability*. These experiments probe fluid mixing, shock heating, and solver accuracy. While by no means exhaustive, they serve to validate the incorporation of the fluid solver into the HACC framework. For a broader investigation of fluid experiments using CRKSPH (and comparisons with other methods), we refer the reader to FRO17. In general, all measurements presented in this section are in close agreement with Spheral,^{††} the code used for the investigations in that work. These results are important as the CRK-HACC framework includes implementation differences compared to Spheral,

for example the use of hierarchical time stepping, which require validation.

4.1.1. Sod Shock Tube

The Sod test (Sod 1978) is a classic 1D Riemann problem used to probe the accuracy and convergence of hydrodynamic codes in the presence of shocks. It studies the evolution of a sharp interface between two gases of differing density and pressure, brought into contact. In general, shock tests violate the inviscid assumption of the SPH fluid equations, wherein artificial viscosity is required to suitably simulate this type of phenomena. Accordingly, the Sod problem provides an appropriate validation test for the viscosity model, especially as it is accompanied by an analytic solution.

Conventionally, the Sod test is measured with one interface at the center of a domain of unit length with reflective boundaries. In our setup, we initialize two Riemann interfaces located at $x = 0.5$ and $x = 1.5$ in a periodic domain $x \in [0, 2)$. This configuration ensures that the resulting shocks will not interfere up to the final time $t = 0.15$, where the measurements are made over the isolated domain $x \in [0, 1)$, effectively replicating the traditional setup.

The transition between the high and low pressure monatomic gases is made continuous by initializing the density and pressure according to

$$f(x) = f_h + (f_l - f_h) \begin{cases} \left[1 + e^{\frac{0.5-x}{\Delta}}\right]^{-1} & x \in [0, 1); \\ \left[1 + e^{\frac{x-1.5}{\Delta}}\right]^{-1} & x \in [1, 2), \end{cases} \quad (54)$$

where f stands for ρ and P , $\rho_h = 1$, $\rho_l = 1/8$, $P_h = 1$, and $P_l = 1/8$ (same temperature on both sides). The interface smoothing scale Δ is set to $\Delta_{\text{low}}/2$, where Δ_{low} is the unperturbed particle spacing in the low density region.

We initialize the 1D problem first, using $\rho_l = 1/2$. To keep constant masses across the interface, we integrate Eq. 54 to determine the target cumulative mass function, which is then inverted to specify the SPH particle positions. At each sample location in the 1D distribution, we then construct a 2D grid of particles in the other dimensions, such that the 3D density matches Eq. 54 with $\rho_l = 1/8$. We remark that CRKSPH does not require a continuous interface to correctly resolve the Sod test, where we find indistinguishable results when using a step-function initial condition.

Fig. 1 shows the properties of the system at time $t = 0.15$ in the isolated domain, as well as the analytic solution. The Sod result includes three primary features, a propagating rarefaction wave (between $x \sim 0.3$ and $x \sim 0.5$), contact discontinuity (density jump at

[†] <https://github.com/arborx/ArborX>

^{††} <https://github.com/LLNL/spheral>

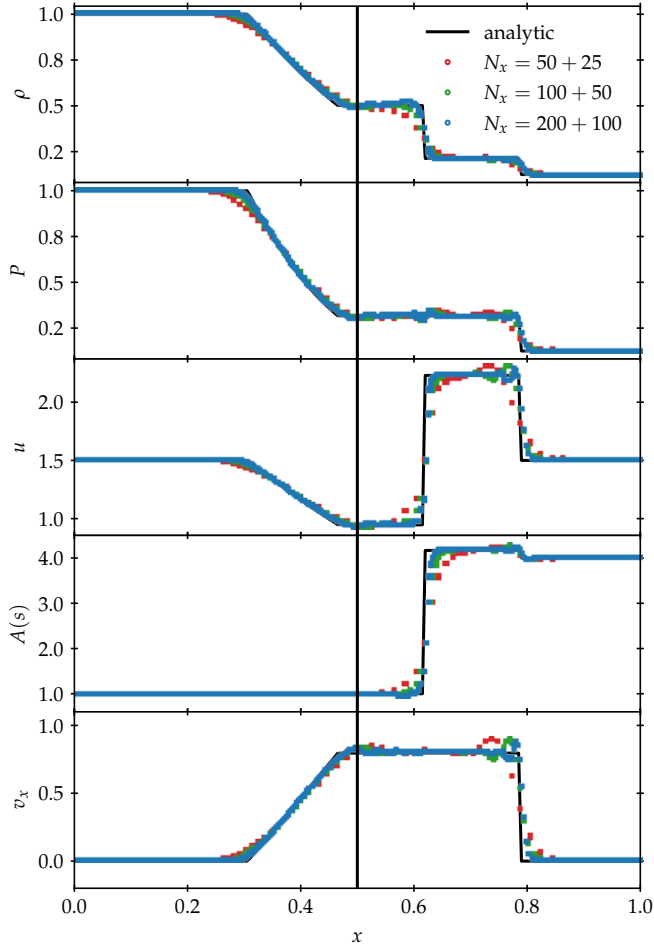


Figure 1. Results of the 3D Sod shock tube test run at $t = 0.15$ with 1D-resolutions of $N_x = 50 + 25$, $100 + 50$, and $200 + 100$ particles across a $[0, 1]$ domain, evenly replicated along the remaining dimensions. The simulations converge to the analytic prediction (black line). Although the panels include all particles, no scatter is visible at each x -coordinate, demonstrating that the 1D solution is well maintained.

$x \sim 0.6$), and shock-front ($x \sim 0.8$). We evolve three resolutions, $N_x = 50 + 25$, $100 + 50$, and $200 + 100$, labeled by the number of particles along the x -axis in the $[0, 1]$ interval, split by the initial Riemann interface. The simulations converge to the analytic prediction with increasing particle count, where the shock-front and contact discontinuity are well resolved. The small scatter (“Gibbs phenomenon”) in velocity, is commonly seen with high order methods near discontinuities, and was measured similarly in FRO17. We emphasize that the figure includes all points in the 3D distribution. No scatter is visible at a given x -coordinate, illustrating that the 1D evolution is preserved in our expansion to three dimensions.

In Fig. 2, we show the L1-norm convergence towards the analytic solution with increasing resolution, fit to

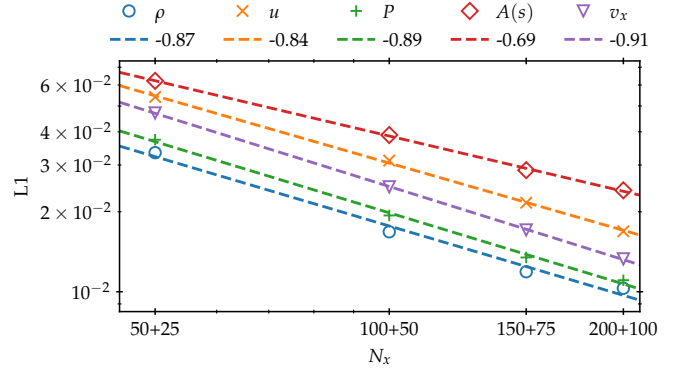


Figure 2. L1-norm convergence of the density, energy, pressure, entropy, and velocity to the analytic solution of the Sod shock tube problem with increasing resolution. The dashed lines show the best-fit power law N^α , with exponents given in the legend. Appropriately, the state-variables converge roughly linearly (N^{-1}), as expected for a shock test.

a power-law N^α . We anticipate first-order convergence (N^{-1}) for problems involving discontinuities, given the inclusion of artificial viscosity. Encouragingly, we find that the deviations of all hydrodynamic quantities scales approximately linearly with resolution, albeit with entropy converging slightly slower than the others.

4.1.2. Sedov-Taylor Blast Wave

The Sedov-Taylor explosion (Sedov 1946; Taylor 1950) simulates a spherical shock generated by the injection of thermal energy in a static uniform background. The difficult setup requires the ability to simulate shock-fronts while simultaneously maintaining spherical symmetry and conservation laws. The blast wave problem has also been used to test the accuracy of hierarchical time step integrators, and served as motivation for the incorporation of time step limiters (Saitoh & Makino 2009), as discussed in Section 3.1.

For our experiment, we initialize equal-mass SPH particles using a glass distribution in a cube of side-length $L = 2$. The density of the monatomic gas is set to unity with null pressure and velocity. At the center of the box, we inject a total energy of $E_0 = 1$ smoothed across half the kernel extent; consistent with FRO17, we have found point-like injections provide qualitatively identical results as the smoothed initial conditions presented here. In total, we set up four different simulations with $N = 64^3, 100^3, 128^3$ and 200^3 particles.

The system is then evolved until the shock-front reaches a radius of $R_{\text{target}} = 0.8$, corresponding to a time $t_{\text{target}} \simeq 0.402$. In the left panel of Fig. 3, we show the particle distribution in a thin slice of depth $\Delta_z = 2/N$ through $z = 0$, colored by the specific energy to differentiate the hot (inside) and cold (outside) gas in regard

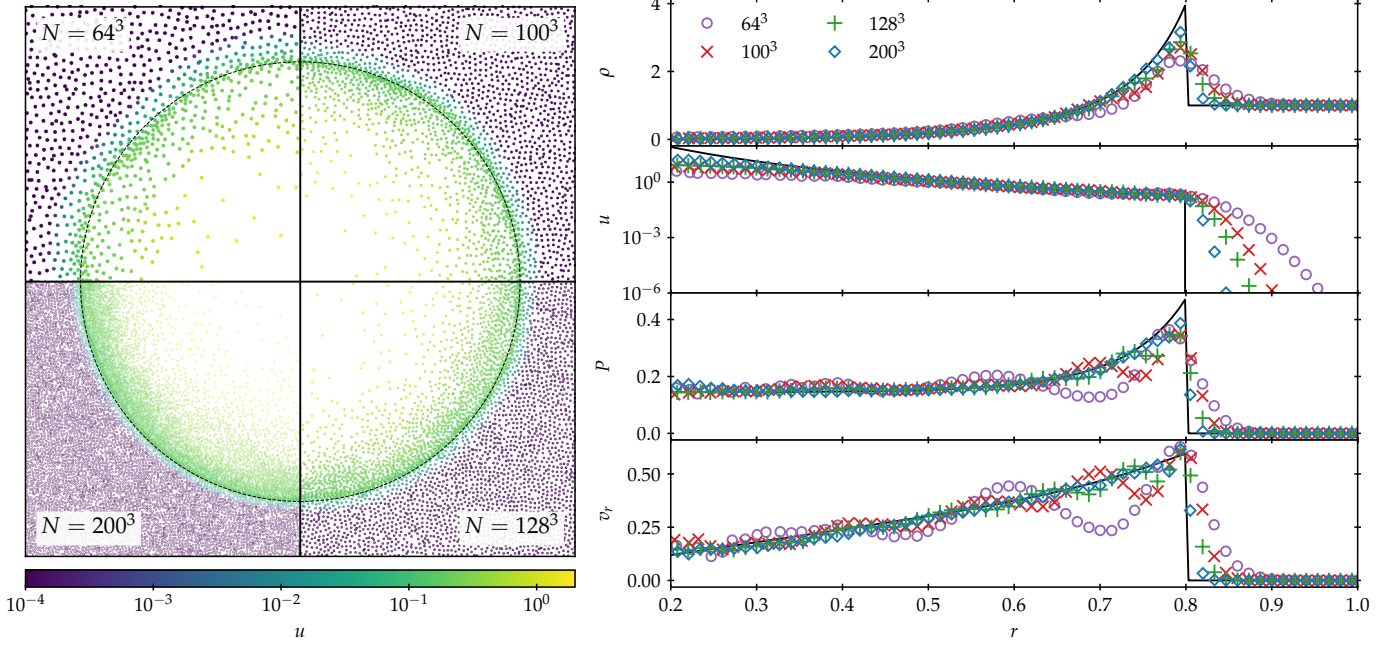


Figure 3. Results of the Sedov-Taylor blast wave problem. **Left:** particle distribution at time $t_{\text{target}} \simeq 0.402$ in a slice of thickness $2/N$, colored by the specific energy u for four different resolution runs. The point size is scaled with the particle mass. **Right:** radial profiles of density, specific energy, pressure and radial velocity, obtained using the median value for each of the 60 bins across a domain $r \in [0.2, 1.0]$. The simulations converge to the analytic solution (black line) at the target time.

to the bubble. The shock wave matches the analytic radius well. In the right panel, we plot the median value of density, specific energy, pressure, and radial velocity measured in evenly spaced radial bins. With increasing resolution, the shock-front is resolved more sharply, and the measured peak density and pressure converge towards the analytic solution. The oscillations of pressure and radial velocity in the post-shock region, a common artifact in SPH codes (see, e.g., Hu et al. 2014; Wadsley et al. 2017), decay as the shock is better resolved. The deviation close to the origin, particularly in the internal energy, is attributed to the difficulty of resolving a near-vacuous solution with low particle sampling.

As was done in the *Sod shock tube test*, we measure the L1-norm convergence in the top panel of Fig. 4; once again, we reassuringly find an approximate N^{-1} power law between the particle data and analytic solution for all properties.

We briefly turn to an investigation of the time step limiter. The middle panel of Fig. 4 shows the ratio of measured L1-norms as a function of limiter level f_l , when compared to simulations where global time stepping was employed. In this experiment the resolution was fixed to $N = 100^3$ particles, with leaf size $N_{\text{ppl}} = 256$. Our results indicate that limiter values $f_l \in [0, 4]$ achieve accurate solutions, where higher levels begin to degrade. This is consistent with the recommendation of Saitoh & Makino (2009) to use $f_l = 2$.

As noted in Section 3.1, our limiters are enforced at the leaf level (rather than particle), and are thus more conservative than the procedure described in Saitoh & Makino (2009). This effect is explored in the bottom panel of the figure, where the limiter is fixed at $f_l = 2$ for the same resolution ($N = 100^3$), and we vary the number of particles per leaf N_{ppl} . We find that using $N_{\text{ppl}} > 16$ particles reaches the noise floor, however the extent that increasing leaf size can assist in the accuracy is limited. We conclude that our default settings of $f_l = 2$ and $N_{\text{ppl}} \in [128, 256]$ used throughout the paper are certainly suitable, if not overly conservative.

4.1.3. Kelvin-Helmholtz Instability

Fluid instabilities play a crucial role in mixing processes and production of turbulence relevant to both astrophysics and general hydrodynamics. The Kelvin-Helmholtz (KH) instability considers a velocity-induced shearing flow across a perturbed fluid interface, and has historically exposed the tendency of traditional SPH methods to suppress fluid mixing (see, e.g., Agertz et al. 2007). The presence of surface tension (“E0”) errors, in addition to the over-activity of traditional artificial viscosity prescriptions, are primary contributors to the erroneous solutions measured with unaltered SPH. As discussed in FRO17, CRKSPH directly addresses these concerns by utilizing accurate reproducing kernels in combination with a novel artificial viscosity treatment, summarized in Section 2.2.

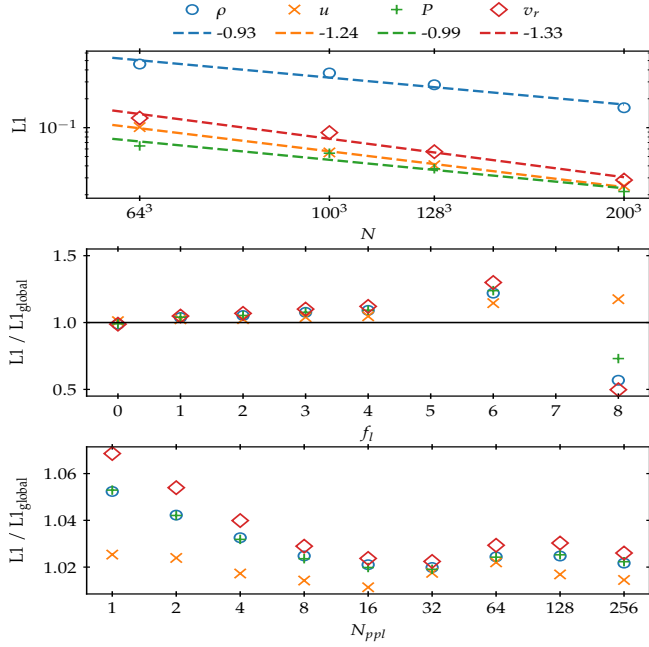


Figure 4. Convergence of the Sedov-Taylor blast wave with respect to the analytic solution. **Default parameters:** $N = 100^3$ resolution, $N_{ppl} = 256$ particles per leaf, $f_l = 2$ limiter level. **Top:** varying resolution **Middle:** varying limiter **Bottom:** varying leaf size. The dashed lines in the top panel show the best-fit power law N^α of the L1-norm for each particle property, with exponents given in the legend; the results exhibit the expected linear (N^{-1}) convergence. The middle and bottom panels measure the L1-norm ratio compared to a simulation with global time stepping at resolution $N = 100^3$; the measurements indicate our default parameter values for f_l and N_{ppl} are conservatively selected.

The KH setup examines the shearing flow across two fluids with differing densities at pressure equilibrium. A single instability mode is excited by adding a velocity perturbation perpendicular to the fluid interface. The shear is converted into vorticity that cascades to turbulence due to secondary instabilities. For our test, we use the smooth KH initial conditions described in McNally et al. (2012). In particular, we place a monatomic gas with uniform pressure $P = 2.5$ in a periodic box with side-length $L = 1$. The interface along the y -axis is characterized by a smooth transition in density (ρ) and x -velocity (v_x), according to

$$f(y) = \begin{cases} f_1 - f_m e^{(y-1/4)/\Delta}, & y \in [0, 1/4]; \\ f_2 + f_m e^{(1/4-y)/\Delta}, & y \in [1/4, 1/2]; \\ f_2 + f_m e^{(y-3/4)/\Delta}, & y \in [1/2, 3/4]; \\ f_1 - f_m e^{(3/4-y)/\Delta}, & y \in [3/4, 1], \end{cases} \quad (55)$$

where f stands for ρ and v_x , $f_m = (f_1 - f_2)/2$, $\rho_1 = 1$, $\rho_2 = 2$, $v_1 = 0.5$, $v_2 = -0.5$, and $\Delta = 0.025$.

A perturbation in the velocity along the y -axis is added as

$$v_y(x) = \delta_y \sin(2\pi x/\lambda), \quad (56)$$

with amplitude $\delta_y = 0.01$ and wavelength $\lambda = 1/2$. The SPH particles are placed on a regular 3D grid with resolutions $N = 64^3$, 128^3 , and 256^3 , using masses initialized by the $\rho(y)$ density constraint, and null velocities in the z -dimension.

Fig. 5 shows the evolved density at $t = 2$ on a slice perpendicular to the z -axis. The vortical roll-ups are induced with increasing detail as the resolution improves. To quantify the convergence, we measure the growth of the y -velocity mixing mode according to the definition in McNally et al. (2012) (Eqs. 10-13 in that reference) and the evolution of the maximum kinetic energy along the y -axis, $E_{\text{kin},y} = \max_i [\frac{1}{2} m_i v_{y,i}^2]$. The quantities are shown in Fig. 6, where we also include the high-resolution results provided by McNally et al. (2012). At low resolution, the amplitude of the y -mode is highly underestimated, especially at late times, which is also visible from the missing vorticity and turbulence in the density snapshot. As the resolution is increased, the y -mode amplitude converges to the McNally et al. (2012) curve. We observe a similar trend in $E_{\text{kin},y}$, however, as the kinetic energy measurement is based on a single particle, it is inherently more noisy than the averaged y -mode amplitude. The scatter feature around $t = 1$ occurs at roughly the classical instability growth rate τ_{KH} (Chandrasekhar 1961), where non-linear effects begin to occur, and has been previously observed in FRO17.

4.2. Gravitation Coupling Experiments

We now consider examples of self-gravitating systems when combined with hydrodynamics. In particular, we present the CRK-HACC solutions for the gravitational (Evrard) collapse of a gas sphere in Section 4.2.1, in addition to a plane-wave Zel'dovich pancake test in a baryon-only universe (Section 4.2.2). We further analyze cosmological cluster simulations in Section 4.2.3, including the well-studied Santa Barbara (Frenk et al. 1999) and nIFTy (Sembolini et al. 2016) cluster comparisons. For a detailed investigation of CRKSPH performance in modeling Keplerian and pressure-supported rotating disks, see Raskin & Owen (2016); accretion disk simulations are insightful tests of angular momentum conservation, where CRKSPH is shown to significantly reduce momentum transport errors compared to a number of SPH prescriptions.

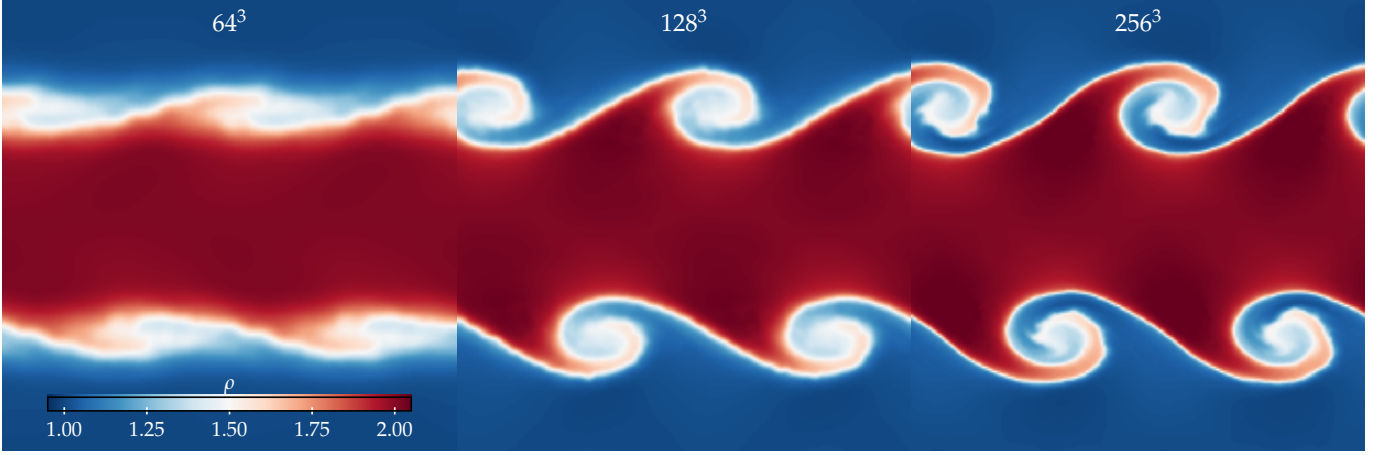


Figure 5. Density field at time $t = 2.0$ for the Kelvin-Helmholtz instability test measured on the xy -plane for $N = 64^3$, 128^3 , and 256^3 particles. At the lowest resolution, the vortices are barely resolved, leading to over-diffusion of the primary instability. With increasing resolution, fluid-mixing is more prevalent, capturing the roll-up of the primary vortices, in addition to secondary instabilities becoming visible.

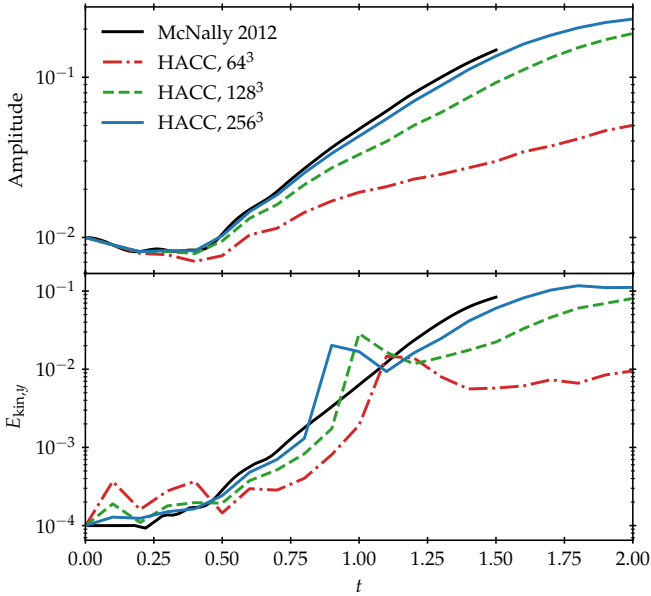


Figure 6. The time-evolution of the y -mode amplitude and the maximum kinetic energy along the y -axis of the Kelvin-Helmholtz instability. In addition to the three HACC-simulations of $N = 64^3$, 128^3 , and 256^3 particles, we include the high-resolution result by [McNally et al. \(2012\)](#). The simulations approach this reference with improving resolution, as the vortices and turbulence are increasingly refined.

4.2.1. Evrard Collapse

The Evrard spherical collapse test is both a simple and instructive self-gravitating experiment extensively used to evaluate astrophysics codes (e.g., [Springel 2010a](#); [Hopkins 2015](#); [Wadsley et al. 2017](#); [Cabezón et al. 2017](#)). The problem, stated in natural units with $G = 1$, considers a spherical gas distribution with an initial $\rho \propto r^{-1}$ density profile that collapses under self-gravity. The re-

sulting heat generated by the compression forms an outwards moving shock. Over the entire evolution, gravitational energy is converted into kinetic and thermal energy, allowing for an insightful test of the interplay between the gravity and hydrodynamic solver, as well as the preservation of conservation laws.

To set up the initial SPH positions, we distort a particle glass distribution such that the density is $\rho(r) \propto r^{-1}$, achieved with a radial transformation $r \mapsto r^{3/2}$.[†] Particles outside a unit sphere are removed, and the equal masses of the remaining points are rescaled such that the total mass is $M = 1$. The monatomic gas is initialized with zero velocity and a uniform specific internal energy of $u = 0.05$. We run the Evrard collapse problem in three resolutions, starting from a $N = 64^3$, 100^3 , and 200^3 glass. The systems are evolved to $t = 2.0$ in a large periodic box of size $L = 90$ to minimize periodicity effects.

Fig. 7 shows the radial properties of the evolved system at time $t = 0.77$. This snapshot was previously studied by [Steinmetz & Mueller \(1993\)](#) who carried out a high-resolution 1D integration in spherical coordinates with a piecewise parabolic method (PPM). We include their results for density, pressure, and radial velocity in the figure. At the sharp shock-front, CRKSPH converges well to the PPM curve with increasing resolution. Outside the shock wave, the measurements are consistent for all resolutions.

In Fig. 8, we show the evolution of the kinetic, thermal, and gravitational energy. We find close agreement

[†] The differential mass in a uniform distribution $dM \propto r^2 dr$ is mapped to a desired mass $dM' \propto r' dr'$, implying a radial transformation $r^2 dr \propto r' dr' \Rightarrow r' \propto r^{3/2}$.

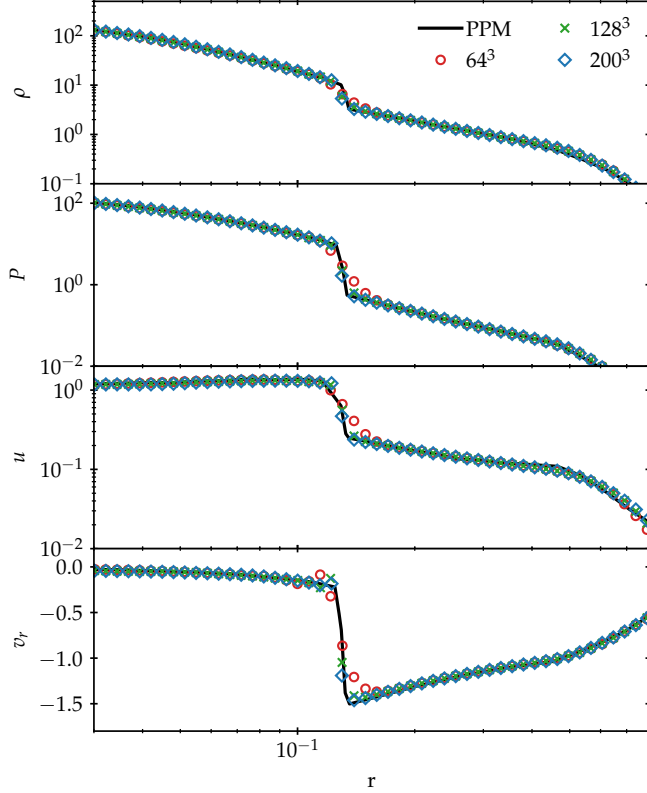


Figure 7. Radial profiles for density, pressure, specific energy, and radial velocity at time $t = 0.77$ for the Evard collapse problem with resolutions $N = 64^3$, 100^3 , and 200^3 particles. The solid line shows the results from the 1D PPM calculation by Steinmetz & Mueller (1993). The simulations converge well with increasing resolution.

with the Steinmetz & Mueller (1993) measurement for all resolutions, with the caveat that the 64^3 simulation slightly underestimates the thermal energy at late times. The results showcase accurate conversion and conservation of energy for the collapse test.

4.2.2. Plane-wave Collapse

Structure in the universe forms through gravitational collapse of primordial density perturbations. The 3-dimensional nature of these random fluctuations results in a process that is anisotropic, where there is a major axis along which these systems collapse first (Zel’dovich 1970). Examining the evolution of a single Fourier mode, i.e., Zel’dovich pancake, allows us to study this phenomenon in an idealized setting (see also Shandarin & Zeldovich 1989).

We consider a diagonal plane-wave collapse in a purely baryonic Einstein–de Sitter universe with $\Omega_m = \Omega_b = 1$, $\Omega_\Lambda = 0$, and $H_0 = 100h \text{ km s}^{-1} \text{ Mpc}^{-1}$. Starting from a uniform Lagrangian distribution, either a grid or glass, in a cube with side-length L , we displace configurations of $N = 128^3$ and 256^3 particles by applying the

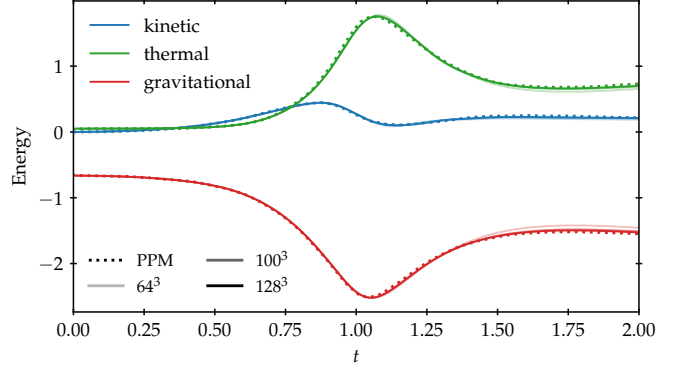


Figure 8. Evolution of the kinetic, thermal, and gravitational energy for the Evard collapse problem. Initially, gravitational potential energy is converted to kinetic in-fall energy, which in turn is shock-heated into thermal energy. As in Fig. 7, CRK-HACC convergences nicely to the 1-D PPM results of Steinmetz & Mueller (1993).

Zel’dovich approximation (Zel’dovich 1970); we use an initial potential of the form $\phi(\mathbf{q}) = -A_\phi \cos(\mathbf{k}\mathbf{q})$, where \mathbf{q} are the Lagrangian coordinates and $\mathbf{k} = 2\pi/L(1, 1, 1)$ is a diagonal wave vector with wavelength $\lambda = L/\sqrt{3}$. The resulting perturbed comoving position \mathbf{x} , velocity $\dot{\mathbf{x}}$, density ρ , and temperature T can be written as

$$\mathbf{x}(\mathbf{q}, a) = \mathbf{q} - A_x a \mathbf{k} \sin(\mathbf{k}\mathbf{q}), \quad (57)$$

$$\dot{\mathbf{x}}(\mathbf{q}, a) = -H_0 a^{-1/2} A_x \mathbf{k} \sin(\mathbf{k}\mathbf{q}), \quad (58)$$

$$\begin{aligned} \rho(\mathbf{q}, a) &= \rho_c (\det d\mathbf{x}/d\mathbf{q})^{-1} \\ &= \rho_c (1 - A_x a \mathbf{k}^2 \cos(\mathbf{k}\mathbf{q}))^{-1}, \end{aligned} \quad (59)$$

$$T(\mathbf{q}, a) = T_0 (\rho/\rho_c)^{\gamma-1}, \quad (60)$$

where $A_x = 2/(3H_0^2)A_\phi$ is the amplitude of the perturbation. Requiring shell-crossing to occur at time a_\times (i.e., $\rho(\mathbf{0}, a_\times) \rightarrow \infty$) implies $A_x = (L/2\pi)^2 (3a_\times)^{-1}$. We initialize the canonical test problem with $\lambda = 64 h^{-1} \text{ Mpc}$, $h = 0.5$, and $a_\times = 0.5$ (consistent with Bryan et al. 1995; Trac & Pen 2004; Springel 2010a; Hopkins 2015) at a starting redshift $z = 200$ and an initial gas temperature $T_0 = 396 \text{ K}$ (corresponding to 100 K at $z = 100$).

In Fig. 9, we show the velocity along the axis of collapse, the gas temperature, and the overdensity at $z = 0$ (well after the crossing time) for both grid and glass initial distributions. In the case of the glass initial conditions, we bin the particles according to their radial distance to the plane of collapse and present the median values of the particle state measurements. For the grid results, we show all particles in the figure, where the lack of visible scatter highlights the preservation of symmetry in the CRKSPH formalism.

For both initial distributions, we find similar convergence with the high-resolution solution of a 1D PPM

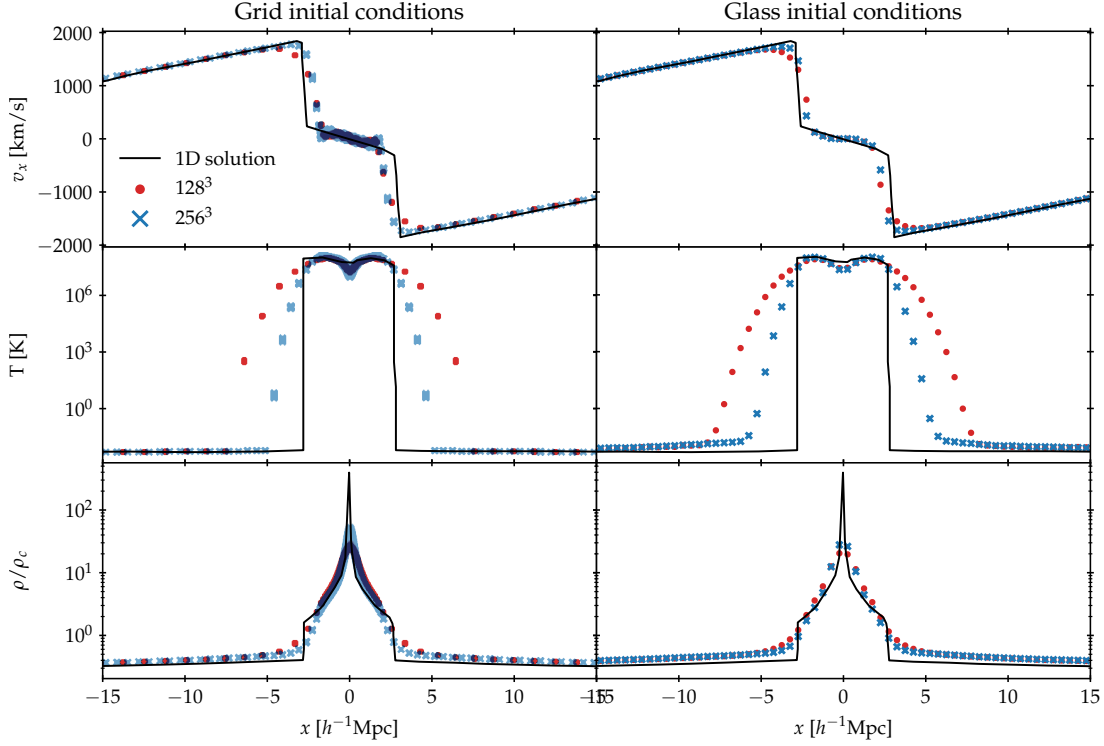


Figure 9. Results of a plane-wave collapse (Zel’dovich pancake) test problem with grid (left) and glass (right) initial conditions. We display the velocity along the plane wave, the gas temperature, and the normalized density at $z = 0$. The grid panel includes all simulation particles, with the lack of scatter indicating that the planar symmetry is preserved throughout the volume. For the glass setup, we show the median values in narrow distance bins perpendicular to the plane of collapse. In black, we include outputs from a high-resolution 1D simulation taken from Hopkins (2015), which the CRK-HACC runs converge towards.

simulation taken from Hopkins (2015); moreover, our results are consistent with the modern SPH glass measurements performed in that work. During shell-crossing, a massive shock is induced that produces a temperature peak many orders of magnitude larger than the cold initial medium. CRKSPH establishes well-behaved velocity profiles of the inner post-shock region, in addition to capturing the shock-fronts favorably with increasing resolution. Outside the active region, the simulations correctly follow the linear solution.

Grid initial conditions for the Zel’dovich pancake are notoriously difficult for Lagrangian codes (given the collapse of a single dimension), and yet, the CRK-HACC solver performs well in the diagonal setting imposed here. In general, CRKSPH demonstrates similar robustness in a number of hydrodynamic problems (as investigated in FRO17), where discontinuous and gridded initial configurations nevertheless yielded accurate results.

4.2.3. Cluster Comparisons

We present results from three sets of cosmological simulations constructed to study profiles of massive clusters. The first example is the well-known Santa Barbara (SB) cluster (Frenk et al. 1999), with initial conditions specified in Heitmann et al. (2005). The setup

evolves $N = 2 \times 256^3$ dark matter plus baryon particles in a box of side-length $L = 32 h^{-1} \text{Mpc}$, at starting redshift $z = 63$. The assumed cosmology is SCDM with $(\Omega_c, \Omega_b, n_s, \sigma_8, h) = (0.9, 0.1, 1.0, 0.9, 0.5)$, where the dark matter and baryon mass resolutions are $m_{\text{DM}} = 4.88 \times 10^8 h^{-1} \text{M}_\odot$ and $m_{\text{gas}} = 5.42 \times 10^7 h^{-1} \text{M}_\odot$, respectively.

A more recent code comparison was performed by the nIFTy collaboration in Sembolini et al. (2016). As opposed to the SB test, with initial conditions chosen to deliberately produce a statistically rare cluster at the center of a small box, the nIFTy setup utilizes the zooming technique of Klypin et al. (2001) to extract a cluster from a larger domain of edge-length $L = 1 h^{-1} \text{Gpc}$. Specifically, the ICs are taken from the MUSIC-2 dataset[†] built from the Multidark simulation (Prada et al. 2012). The cosmology is WMAP-7+BAO+SNI (Komatsu et al. 2011) with $(\Omega_m, \Omega_b, \Omega_\Lambda, n_s, \sigma_8, h) = (0.27, 0.0469, 0.73, 0.95, 0.82, 0.7)$. Gravity-only and hydrodynamic runs were both performed, which correspond to a mass resolution of $m_{\text{DM}} = 1.09 \times 10^9 h^{-1} \text{M}_\odot$.

[†] <https://music.ft.uam.es/>

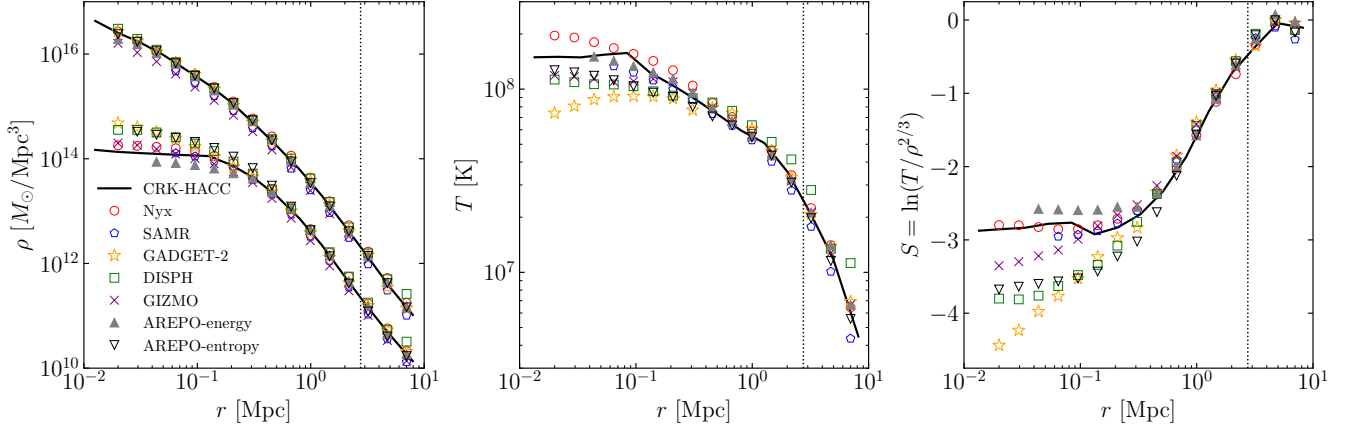


Figure 10. Radial profiles showing density (left), temperature (center), and entropy (right) for the Santa Barbara cluster (Frenk et al. 1999) at redshift $z = 0$ for a number of Lagrangian (CRK-HACC, GADGET-2, DISPH), Eulerian (Nyx, SAMR), and hybrid (GIZMO, AREPO) solvers. In the case of AREPO we show results from both the strict energy conservation and dual entropy formulations. The lower (upper) set of data points in the left panel correspond to the baryon (dark matter) density profile, while the vertical dotted line in each panel denotes $R_{200} = 2.75$ Mpc. Notably, the CRK-HACC measurements are consistent with the grid-based approaches.

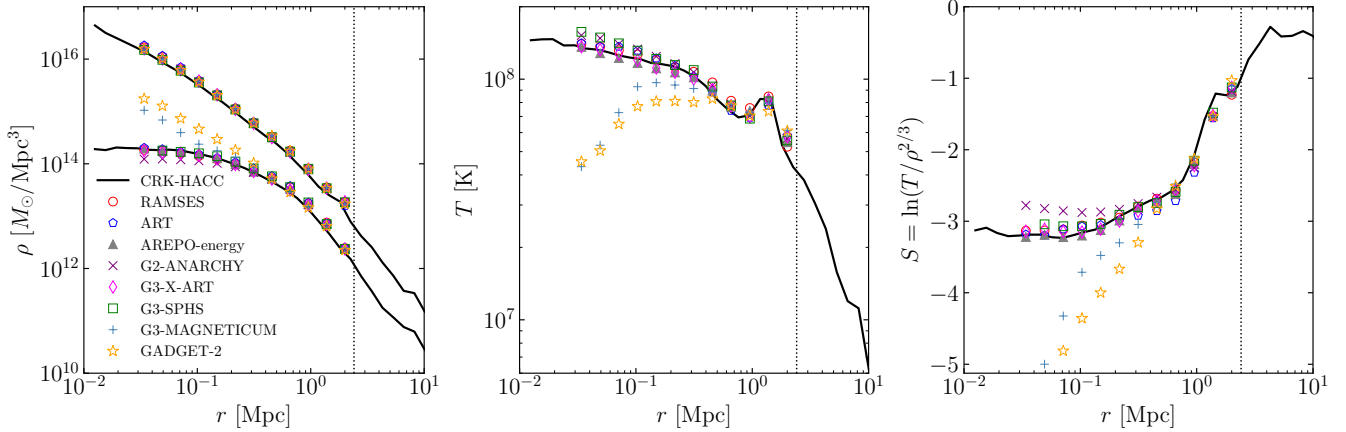


Figure 11. Radial profiles showing density (left), temperature (center), and entropy (right) for the nIFTy cluster (Sembolini et al. 2016) at redshift $z = 0$ for a variety of Lagrangian (CRK-HACC, GADGET-2, G2-ANARCHY, G3-X-ART, G3-SPHS, G3-MAGNETICUM), Eulerian (RAMSES, ART), and hybrid (AREPO) solvers. The lower set of data points in the left panel correspond to the baryon density profile from the non-radiative run while the upper set of points correspond to the total matter density profile in the gravity-only run. In each panel the vertical dotted line denotes the halo radius, $R_{200} = 2.41$ Mpc, identified with CRK-HACC. As opposed to the discrepancies seen in Fig. 10, most of the methods are in closer relative agreement for the nIFTy comparison. The CRK-HACC results are again consistent with the mesh-codes, and are amongst the grouping of modern SPH codes.

for the former, and $m_{\text{DM}} = 9.01 \times 10^8 h^{-1} M_{\odot}$ and $m_{\text{gas}} = 1.9 \times 10^8 h^{-1} M_{\odot}$ for the latter.

The final simulation is called the Argonne cluster, which represents a modern version of the SB setup to be used for convergence studies. The initial conditions follow the procedure of Hoffman & Ribak (1991), similar to the SB arrangement. We employ the best-fit WMAP-7 Λ CDM cosmology with $(\Omega_c, \Omega_b, \Omega_{\Lambda}, \Omega_{\nu}, w, n_s, \sigma_8, h) = (0.22, 0.0448, 0.7352, 0, -1, 0.963, 0.8, 0.71)$ in a volume of width $L = 64 h^{-1} \text{Mpc}$. The ICs seed a random field at $z = 200$ on a 2048^3 grid to accommo-

date particle counts up to 2×1024^3 without incurring interpolation error from the finite mesh. Initial configurations for $N = 2 \times 128^3$, 2×256^3 , and 2×512^3 particles have been made publicly available for comparison.[†] The mass resolution of the middle (2×256^3) run corresponds to a dark matter mass $m_{\text{DM}} = 9.54 \times 10^8 h^{-1} M_{\odot}$, and baryon mass $m_{\text{gas}} = 1.94 \times 10^8 h^{-1} M_{\odot}$.

[†] <https://cosmology.alcf.anl.gov/static/ArgonneCluster/ICs>

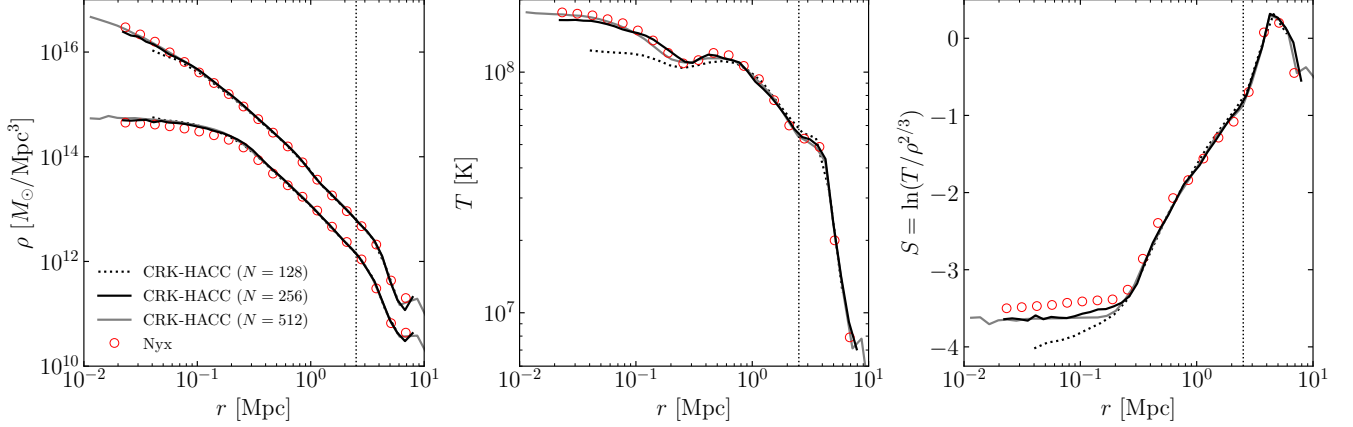


Figure 12. Radial profiles showing density (left), temperature (center), and entropy (right) for the Argonne cluster run at redshift $z = 0$. The lower (upper) set of data points in the left panel correspond to the baryon (dark matter) density profile, while the vertical dotted line in each panel denotes $R_{200} = 2.52$ Mpc found by CRK-HACC. As in Fig. 10, the CRK-HACC solutions are closely consistent with the Eulerian approach (Nyx), where the results appear to be numerically converged.

We begin with an investigation of the SB cluster. The simulation ran with a gravitational softening length set to $r_{\text{soft}} = 1.25 h^{-1}\text{kpc}$. The main cluster was extracted using an FOF algorithm applied only to the dark matter particles. Spherical shells were built outwards from the gravitational potential center in order to construct radial profiles for both particle species. The radius at which the interior density falls below $200\rho_c$ was found to be $R_{200} = 2.75$ Mpc with an enclosed mass of $M_{200} = 1.21 \times 10^{15} M_{\odot}$. These numbers are in agreement with the values reported in Frenk et al. (1999) measured for a variety of solvers, albeit on the upper range of the data. As described in that work, cluster property measurements, in general, have all been found to be reasonably consistent among the different codes studied.

Radial profiles for density, temperature, and entropy of the SB cluster at $z = 0$ are shown in Fig. 10. We have included measurements pulled from the literature for a number of cosmological codes that employ a diverse set of hydrodynamic solvers. In particular, we compare results for Eulerian AMR methods (Nyx; Almgren et al. 2013, SAMR; Frenk et al. 1999), Lagrangian SPH schemes (GADGET-2; Springel 2005, DISPH; Saitoh & Makino 2016), and hybrid approaches (GIZMO; Hopkins 2015, AREPO; Springel 2010a). In the case of GIZMO, we show the profiles produced by the meshless finite-mass (MFM) solver, and for AREPO we consider both the strict energy conservation and dual entropy formulations (marked appropriately in Fig. 10).

Consistent with the findings of Frenk et al. (1999) and subsequent investigations, the range of methods agree on both the complete dark matter profile, and gas measurements outside the cluster central region ($r \gtrsim 0.5$ Mpc). However, for the inner domain ($r \lesssim 0.5$ Mpc), devi-

ations between solvers are apparent, the most prominent being the entropy profile; these conflicts have not been resolved with increasing resolution (e.g., Mitchell et al. 2009). As traditionally observed, the Eulerian solvers (Nyx and SAMR) demonstrate a systematically higher entropy “core,” as opposed to the unmodified SPH codes (GADGET-2). These tensions have been somewhat alleviated by modern SPH methods (DISPH) and hybrid approaches (AREPO-entropy and GIZMO), however, there is still a significant offset in magnitude. Interestingly, CRK-HACC appears to produce consistent measurements with the mesh-based approaches, in contrast to the other schemes.

One partial explanation for the discrepancy of the solvers (e.g., Springel 2010a; Hopkins 2015), is the adherence of SPH codes to fluid mixing, thus suppressing the entropy profile. Additionally, it is further argued that grid codes are more susceptible to artificial heating, seeded by noise from the gravity solver, as well as over-mixing and diffusing entropy. In accordance, observe the AREPO-energy solution in Fig. 10, the subject of which is described in detail in Springel (2010a). Briefly, by disabling a dual entropy/energy switch used to suppress artificial heating incurred by cold fluids moving at a high Mach number, AREPO will generate similar entropy profiles as grid codes, supporting the claim that these cores originate from numerical processes. These results are reaffirmed in the findings of Hopkins (2015), where GIZMO can artificially recover the entropy cores by introducing enhanced diffusion via shutting off similar entropy/energy switches. The conservative conclusion of these examinations would be that the “true” solution lies between the unmodified SPH and Eulerian profiles, however, the degree to which is unclear.

Despite these conjectures, CRK-HACC appears to produce consistent measurements with the mesh-based approaches without any modifications. Indeed, one of the benefits of the CRKSPH solver is the improvement of fluid mixing in SPH simulations, although the extent to which it agrees with the Eulerian codes is notable. It is insightful to compare the CRK-HACC results with DISPH. Similar to the CRKSPH methodology, DISPH utilizes a modern version of artificial viscosity, and promotes improved fluid mixing by utilizing energy-based SPH weighting functions (see [Hopkins 2012](#) for a generalized description of this approach). Unsurprisingly, DISPH demonstrates improved solutions for the SB cluster, with profiles similar to AREPO-entropy, yet does not fully realize entropy cores as CRK-HACC does.

A critical observation was made in [Saitoh & Makino \(2016\)](#), where DISPH could be altered to agree with the Eulerian codes if it included artificial conductivity treatments – a common approach that introduces dissipation to smooth discontinuities in thermal energy (e.g., [Price 2008](#)), akin to viscosity models for kinetic energy. In fact, multiple earlier studies have concluded that artificial conductivity can resolve the entropy profile tensions for SPH methods (e.g., [Wadsley et al. 2008](#); [Read & Hayfield 2012](#); [Power et al. 2014](#); [Biffi & Valdarnini 2015](#); [Hopkins 2015](#); [Beck et al. 2016](#)). While some of these investigations required unphysical conductivity models, which in turn degraded the SPH scheme, others found sophisticated switches to improve these effects. The culmination of this effort is conveyed well by the nIFTy comparison cluster, which we illustrate in Fig. 11.

Similar to the SB project, the nIFTy collaboration includes results from a number of modern cosmology solvers. For comparison, we extracted profiles for both grid-based approaches (RAMSES; [Teyssier 2002](#), and ART; [Rudd et al. 2008](#)) and “modern” SPH variants of GADGET (G2-ANARCHY; see Appendix A in [Schaye et al. 2015](#), G3-X-ART; [Beck et al. 2016](#), G3-SPHS; [Read & Hayfield 2012](#), and G3-MAGNETICUM; [Hirschmann et al. 2014](#)). We further include AREPO-energy and GADGET-2 (referred to as G2-X in [Sembolini et al. 2016](#)) as was done in our previous SB investigation. The AREPO-entropy formulation was not utilized in this study.

Fig. 11 shows the radial profiles, where we measured the halo mass to be $M_{200} = 1.59 \times 10^{15} M_{\odot}$ with $R_{200} = 2.41$ Mpc. While the traditional SPH approach once again displays similar tensions with the Eulerian codes for the entropy profile, a majority of the modern methods are in relative agreement, including the CRK-HACC results. However, there were a couple of SPH methods in the nIFTy investigation that produced sup-

pressed profiles (e.g., the G3-MAGNETICUM solution in Fig. 11). The primary listed contributor to the discrepancy is differing sophistication of artificial conductivity models. In fact, all of the modern SPH approaches required some form of conductivity to achieve their results, as described above.

In light of this fact, the CRK-HACC findings are intriguing. The CRKSPH framework displays consistent profiles with the other methods, yet it does not include conductivity in the hydrodynamic solver. While conductivity would be simple to add to the CRKSPH methodology, we chose to avoid the dangers of potentially resolving unphysical entropy transport – particularly as our fluid and self-gravitating experiments do not indicate a necessity for it (similarly stated in [FRO17](#)).

To conclude, we briefly inspect the convergence of the CRK-HACC results, to ensure that the SB and nIFTy measurements are not seeded by unresolved numerical artifacts. We utilize the Argonne cluster for this purpose, simulated with both CRK-HACC and the AMR code Nyx. In the case of CRK-HACC, we performed convergence runs of $N = 2 \times 128^3$, 2×256^3 , 2×512^3 dark matter plus baryon particles and set the gravitational softening length to $1/16$ the mean inter-particle separation ($r_{\text{soft}} = 15.6 h^{-1} \text{kpc}$). Regarding Nyx, we ran using $N_{\text{DM}} = 256^3$ dark matter particles in conjunction with a hydro mesh of extent $N_{\text{cell}} = 256^3$ that allowed for 4 levels of grid refinement.

Fig. 12 shows radial profiles of the Argonne cluster at $z = 0$ for both codes. The halo mass is calculated to be $M_{200} = 1.88 \times 10^{15} M_{\odot}$ with $R_{200} = 2.52$ Mpc. Reassuringly, we find that the internal profiles measured between CRK-HACC and Nyx are in close agreement. While the smallest simulation slightly undershoots the Nyx entropy core, the higher resolution CRK-HACC runs match well. Thus, CRK-HACC appears to be numerically converged to a consistent solution with Eulerian solvers, and achieves this result without the use of artificial conductivity. We intend to investigate these findings further in the future, where we suspect the explanation is likely connected to the compatible energy formalism in CRKSPH.

5. SCALE-FREE COSMOLOGY SIMULATIONS

Validation of cosmological simulations is complicated by the inherently non-linear evolution of gravitational collapse, precluding an analytic prediction. However, imposing scale-free initial conditions results in self-similar structure formation, where conformance to theoretical scaling relations can be measured to uniquely probe solver accuracy. This methodology pairs well with standard code comparisons, such as the investigations of

the previous section, which provide guidance in gauging the relative systematic variances between different numerical methods.

The theoretical motivation for self-similar solutions traces back to the early results of [Efstathiou et al. \(1979\)](#) as well as derivations in [Peebles \(1980\)](#). Further, [Kaiser \(1986\)](#) studied the application of similarity to predict the evolution of galaxy clusters. In general, scale-free simulations have a long history in N-body measurements (e.g., [Efstathiou et al. 1988](#); [Colombi et al. 1995](#); [Jain & Bertschinger 1998](#); [Smith et al. 2003](#); [Widrow et al. 2009](#); [Ludlow & Angulo 2016](#); [Benhaïem et al. 2017](#); [Joyce et al. 2021](#) to name a few).

The concept is to construct a cosmological simulation where the only relevant physical scale is the amplitude of density fluctuations. Following the approach outlined in [Owen et al. \(1998a\)](#), this can be achieved by instantiating a particle distribution in an Einstein–de Sitter (EdS) universe that is displaced by a Gaussian random field of initial power spectra

$$P(k) = A_0 k^{n_s}, \quad (61)$$

with normalization A_0 and spectral index n_s . The initial conditions and background growth are both free of any physical scale, and, therefore, produce self-similar growth in time. Moreover, we expect numerical artifacts to not obey the theoretical scaling relations, where measurements of departure from self-similarity can highlight the spatial resolution limitations of a solver.

We focus here on simulations with gravity and non-radiative hydrodynamics, as both phenomena do not introduce any additional fundamental scales. One can further expand this approach to model radiative gas, which is explored for a particular family of power-law cooling functions in [Owen et al. \(1998b\)](#). The subsequent analysis is restricted to similarity measurements of integrated halo properties and profiles, where we aim to quantify the adherence to predicted scaling relations of hydrodynamic quantities.

To determine self-similarity, we first need to identify the underlying (non-linear) gravitational collapse scale, where we denote measurements with an asterisk; namely, mass (M_*), density (ρ_*), radius (R_*), temperature (T_*), and entropy (S_*). Due to the hierarchical nature of structure formation, the non-linear extent will increase with time. Self-similarity dictates that objects normalized by the collapsed scales will match corresponding structures at later times. For instance, the scaled temperature, $T/T_*(t)$, should agree for halos of fixed scaled mass $M/M_*(t)$ (but not fixed M) at all times t . While technically we still lack analytic predictions to compare the structure of specific collapsed

objects, we now are capable of confirming temporal self-similarity over the entire evolution.

In the following analysis, we employ a scale-free cosmological simulation to investigate self-similarity using the combined gravity and non-radiative hydrodynamic solvers in CRK-HACC. The simulation contains $N = 2 \times 512^3$ dark matter plus baryon particles in a box of width $L = 40 h^{-1} \text{Mpc}$, with corresponding mass resolutions $m_{\text{DM}} = 1.06 \times 10^8 h^{-1} M_\odot$ and $m_{\text{gas}} = 2.65 \times 10^7 h^{-1} M_\odot$. The initial conditions are set at $z = 200$ using a power-law power spectrum (Eq. 61) with spectral index $n_s = -2$ and normalization determined by $\sigma_8 = 0.5$. The cosmology is specified by an EdS universe with $\Omega_b = 0.2$, $\Omega_c = 0.8$, and $h = 0.5$. The gravitational softening length is fixed to $r_{\text{soft}} = 4.88 h^{-1} \text{kpc}$, and we use COSMOTOOLS (see Section 3.8) to identify SO halos with $\Delta_c = 200$ relative to the critical density of the universe at a range of simulation snapshots.

We begin the investigation in Section 5.1, by providing a derivation of the scaling relations imposed by scale-free initial conditions. We then use a gravity-only simulation in Section 5.2 to determine the resolution limits where self-similarity breaks down due to numerical artifacts. Finally, we present self-similar measurements when hydrodynamics is additionally modeled in Section 5.3.

5.1. Scaling Relations

The following derivation of the non-linear scale quantities (e.g., M_*) considers specifically a spectral index $n_s = -2$; however, the procedure follows identically for any arbitrary choice of n_s . By definition, M_* is inferred from the scale at which gravitational collapse occurs. The spherical collapse model in an EdS universe predicts this scale is reached for density perturbations above a critical value of $\delta_c = 1.686$ ([Lacey & Cole 1993](#)). We can calculate $M_*(a)$ by smoothing the linear density field with filters of varying mass to measure where the density first exceeds δ_c .

We follow the approach outlined in [Lacey & Cole \(1993\)](#), whereby the variance in the density field for mass scale M is computed by integrating over the power spectrum $P(k, a)$ filtered with a spherical kernel of radius $R(M)$:

$$\sigma^2(M, a) = \frac{1}{2\pi^2} \int_0^\infty k^2 P(k, a) W[R(M)k]^2 dk. \quad (62)$$

Here, $W(x) \equiv (3/x^3)(\sin x - x \cos x)$ is the filter, and $R(M) = (3M/4\pi\bar{\rho})^{1/3}$, with $\bar{\rho}$ denoting the mean matter density of the universe. We can simplify this expression by substituting $P(k, a) = a^2 A_0 k^{-2}$, where we make use of the fact that the growth factor is simply a in an EdS universe. In the case where $n_s = -2$, we are left

with an integral over the filter function $\int_0^\infty W(Rk)^2 dk = 3\pi/(5R)$, allowing us to write

$$\sigma^2(M, a) = \frac{3a^2 A_0}{10\pi R(M)}. \quad (63)$$

The normalization A_0 is determined by imposing the constraint that $\sigma^2(M, 1)$ evaluates to σ_8^2 when smoothed on the length scale $R = 8 h^{-1}\text{Mpc}$. With this requirement, we find that $A_0 = 80\pi\sigma_8^2/3$ and, thus, arrive at the final result:

$$\sigma^2(M, a) = a^2 \frac{8\sigma_8^2}{R(M)}. \quad (64)$$

The non-linear mass scale is evaluated by setting $\sigma^2(M_*, a) = \delta_c^2$ and solving Eq. 64 for M_* . We then associate M_* with a density scale, ρ_* , by making the assumption that the non-linear mass collapses to form spherical objects with an overdensity Δ_c . We choose a value of $\Delta_c = 200$ to facilitate comparisons with the convention used in our halo-finder, though we note that the exact choice of Δ_c is unimportant in terms of identifying self-similar relations. The length scale R_* is set as the radius of a sphere of mass M_* and density ρ_* , while the non-linear temperature is taken to be the virial quantity $T_* = (\mu m_p)/(2k_B)(GM_*/R_*)$. For the molecular weight μ , we assume a constant value of $\mu = 0.59$ for fully ionized gas. Finally, entropy is calculated following the definition $S_* = \ln(T_*/\rho_*^{2/3})$. Evaluating all of these relations for the use case of $\sigma_8 = 0.5$ yields the following results expressed in proper units:

$$\begin{aligned} M_* &= 4.05 \times 10^{11} a^6 h^{-1} M_\odot, \\ \rho_* &= 5.55 \times 10^{13} a^{-3} h^2 M_\odot \text{Mpc}^{-3}, \\ R_* &= 0.12 a^3 h^{-1} \text{Mpc}, \\ T_* &= 5.19 \times 10^5 a^3 \text{K}, \\ S_* &= -7.94 + 5\ln(a). \end{aligned} \quad (65)$$

With the scaling quantities defined, we now proceed with an analysis of the convergence limits in the scale-free simulations.

5.2. Convergence Limits

The objective of this investigation is to provide measurements of temporal self-similarity for halos spanning a broad range in both mass and time. As mentioned previously, the finite resolution of numerical simulations will introduce non-physical artifacts that violate the assumptions required for self-similar growth. Therefore, we must first determine a minimum length R_{conv} and mass M_{conv} at which we would expect to find converged measurements of self-similarity.

An evident non-physical measure introduced in the simulation is the gravitational softening length, r_{soft} . Another related characteristic scale is the extent at which mass segregation effects occur due to the artificially strong gravitational forces between the light baryon and heavy dark matter particles (e.g., [Efstathiou & Eastwood 1981](#); [Binney & Knebe 2002](#); [Power et al. 2016](#); [Emberson et al. 2019](#)). The hydrodynamic force resolution set by the SPH neighbor count also introduces a nonphysical scale, albeit one that is spatially adaptive to the local baryon density. Based on the analysis in [Emberson et al. \(2019\)](#), we expect that the coarsest of these limitations is set by mass segregation, which was reported to occur at lengths a few times larger than r_{soft} , as well as in halos containing fewer than roughly three thousand particles.

A straightforward way to measure the scales impacted by mass segregation is to perform a gravity-only simulation. In this case, we expect the baryons to trace the dark matter, as they both follow the same gravitational evolution. Hence, the baryon fraction measured within halos should equal the universal mean, $f_b = \Omega_b/\Omega_m$, and any departures from this value will signify that those scales have failed to converge due to numerical artifacts. Therefore, to obtain a measure of the converged quantities R_{conv} and M_{conv} , we run a gravity-only realization with the same initial conditions as the non-radiative target simulation. We then measure the baryon fraction within halos and use departures from the mean value to set the convergence limits in our analysis.

In the top panel of Fig. 13, we show radial profiles of the baryon fraction stacked over halos in different mass bins. To avoid potential scatter from major merger events, we consider only relaxed halos for which the halo potential minimum and center of mass deviate by no more than 7% of the SO radius R_{200} . The result is that the four largest mass bins agree well with the universal baryon fraction at $r \sim R_{200}$ but show a steady decline in f_b with decreasing radius. The vertical dotted lines indicate a fixed length of $5r_{\text{soft}} = 24.4 h^{-1}\text{kpc}$ for each mass bin, highlighting a roughly constant physical deviation scale. For the four largest mass bins, this scale approximately separates where the baryon fraction begins to diverge at the percent level from the universal mean. Therefore, we set $R_{\text{conv}} = 24.4 h^{-1}\text{kpc}$ as the minimum converged length scale in our simulations.

It is important to recognize that the lowest mass bin in the top panel of Fig. 13 deviates from the universal baryon fraction on scales larger than $R_{200} > R_{\text{conv}}$. In this case, the lack of convergence is related to insufficient particle sampling to constrain the mass segregation to the halo core. We examine this explicitly in the bot-

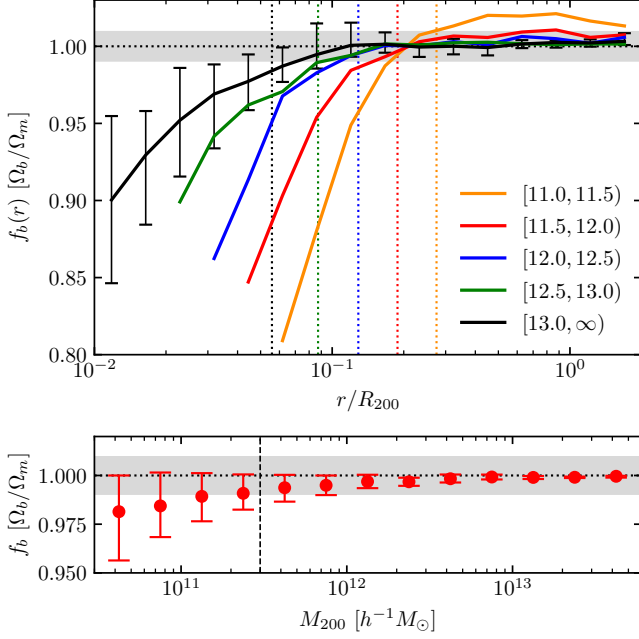


Figure 13. (Top) Radial profiles of the baryon fraction normalized to the universal mean at $z = 0$ for the gravity-only scale-free simulation. The solid colored lines trace the median profile for halos stacked in five mass bins. The legend lists the bin widths in units of $\log(M_{200})$. For the most massive bin, we also show the 25th and 75th percentiles from the stack as error bars. The vertical dotted lines indicate the location of the convergence length $R_{\text{conv}} = 24.4 h^{-1} \text{kpc}$ for each mass bin of the corresponding color. (Bottom) Global baryon mass fraction in units of the universal mean as a function of M_{200} at $z = 0$. The red circles denote the median in each bin, while the error bars show the 25th and 75th percentiles of the distribution. The vertical dashed black line indicates the converged mass scale $M_{\text{conv}} = 3 \times 10^{11} h^{-1} M_{\odot}$. In both panels, the gray shaded band highlights $\pm 1\%$ deviations from the universal mean.

tom panel of Fig. 13, where the global baryon fraction is measured as a function of halo mass. It is apparent that large mass halos agree well with the universal mean while the smallest objects are systematically low. From this result, we set the minimum converged mass to $M_{\text{conv}} = 3 \times 10^{11} h^{-1} M_{\odot}$, which corresponds to ~ 2300 times the combined dark matter plus baryon particle mass. With R_{conv} and M_{conv} determined, we now investigate self-similar scaling when coupling the hydrodynamic force solver.

5.3. Self-similar Measurements

For our final examination, we explore temporal self-similarity of integrated halo measurements, as well as spherically averaged radial profiles for the non-radiative scale-free simulation. In accordance with the previous section, we include only relaxed halos, discard masses

below $M_{\text{conv}} = 3 \times 10^{11} h^{-1} M_{\odot}$, and truncate radial profiles below $R_{\text{conv}} = 24.4 h^{-1} \text{kpc}$. If this selection process successfully mitigates the contributions from numerical artifacts, we expect to find self-similar evolution over all remaining mass and length scales.

We begin with an investigation of the global density, temperature, and entropy integrated over the full halo volume. In the case of density, we specifically measure the baryon component, $\rho_b = 3M_{200,b}/(4\pi R_{200}^3)$, where $M_{200,b}$ is the baryon mass contained within R_{200} . Regarding temperature, we calculate the mass-weighted average of all baryon particles within the halo, which in turn determines the entropy as $S = \ln(T/\rho_b^{2/3})$. To gauge self-similarity of the integrated measurements, we use the following procedure.

At each simulation snapshot, we separate the halos into scaled mass bins that are evenly distributed in log space by $\Delta \log(M/M_*) = 0.1$ (henceforth M denotes M_{200}). For bins containing at least 10 halos, we record the mean and standard deviation σ of the integrated density, temperature, and entropy normalized by the corresponding non-linear values listed in Eq. 65. Finally, we collect results over all snapshots and discard any mass bins that do not contain at least two redshift samples.

The outcome of this procedure is shown in Fig. 14. For each integrated quantity, we plot the mean value of a given mass bin at multiple redshifts listed in the legend. We further average each bin over all corresponding redshift values and trace the result with a solid black curve. Similarly, the gray shading centered on the curve denotes the standard deviation obtained in quadrature from the individual σ -measurements at each redshift.

The test for self-similarity is determined by considering each fixed M/M_* mass bin and confirming that the individual redshift samples are in reasonable agreement. To facilitate this comparison, the bottom panels of Fig. 14 show the ratio of individual redshift measurements and the averaged value in each bin. For almost all normalized masses, we find that the redshift samples are well contained within their combined 1σ scatter. The variation in ρ_b/ρ_* , T/T_* , and $S - S_*$ is roughly 1%, 5%, and 2%, respectively. The mass bins with the highest constraints on self-similarity are those with the most overlapping redshift samples; in particular, mass bins near $M/M_* \simeq 20$ contain the five lowest redshift values, ranging from $z = 0$ up to $z = 0.67$. From Eq. 65, $M_* \propto a^6$, indicating that halos within these bins differ by a factor of ~ 20 in mass.

We reiterate that the analysis is performed on halos at fixed M/M_* , and that the scale-free setup does not generally predict self-similar growth of objects at differ-

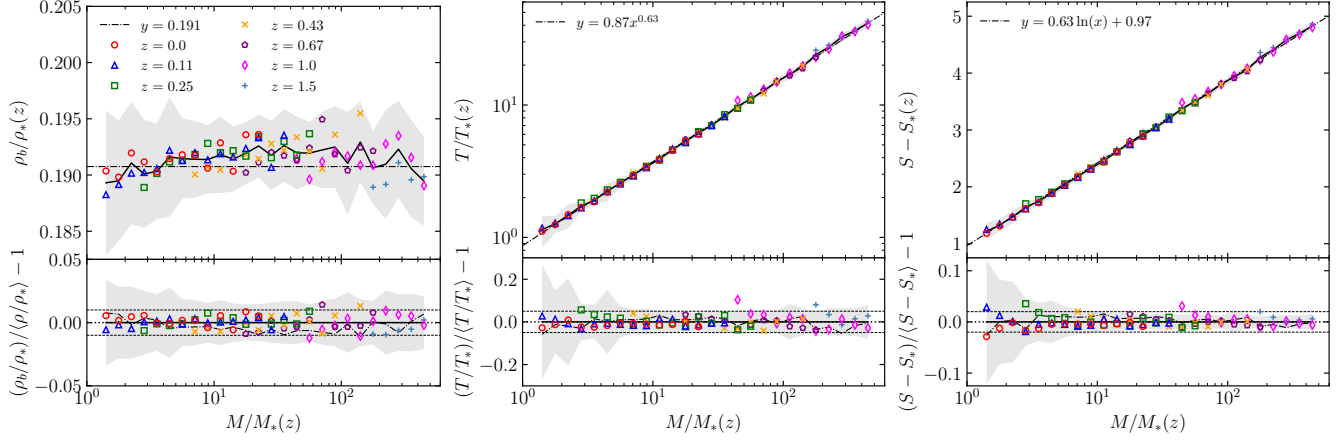


Figure 14. Integrated halo baryon density (left), temperature (center), and entropy (right) normalized to the corresponding non-linear scale defined in Eq. 65 for redshifts listed in the legend. Each marker denotes the mean value for all halos in a given redshift and mass bin consisting of at least 10 halos. We only include results from bins containing more than one redshift sample. The solid black line traces the mean value of each bin for all redshifts, while the shaded gray band shows the corresponding standard deviation. The dash-dotted black line represents a least-squares regression fit of the data for each quantity. The bottom panel shows the ratio of all measurements to the mean curve, where the horizontal dashed lines indicate a $\pm 1\%$, $\pm 5\%$, and $\pm 2\%$ spread for the left, center, and right panels, respectively.

ent M/M_* values. Nevertheless, in cosmological simulations, halos tend to evolve into characteristic density profiles (Navarro et al. 1997) where it is reasonable to assume that some level of self-similarity will exist across mass bins. In fact, this assumption has been used in the past to model the evolution of galaxy clusters (e.g., Kaiser 1986). To determine the extent of similarity across different mass bins, we can measure the scaling behavior across each M/M_* sample.

The result of this investigation is characterized by the black dash-dotted lines in Fig. 14, which represent fitted scaling relations made across M/M_* bins. Regarding density, the data is well approximated by a constant ratio of $\rho_b/\rho_*(z) = 0.191$. Given that the universal mean baryon fraction is $\Omega_b/\Omega_m = 0.2$, halos in the scale-free simulation are evolving to a constant proportion $f_b = 0.191/0.2 = 0.955$. Interestingly, this finding is consistent with the f_b measurements produced by the cosmological non-radiative *Borg Cube* simulation, which were recorded to be $\sim 95\%$ that of the universal mean (Emberson et al. 2019). For temperature, the power-law $T/T_* = 0.87(M/M_*)^{0.63}$ tightly characterizes the data, which is in close agreement with the relation $T/T_* \propto (M/M_*)^{2/3}$ that one would expect if self-similarity was assumed to hold across M/M_* [†]. A comparable result was observed in the $n_s = -1$ scale-free simulations of Owen et al. (1998a), who found a mass-temperature power-law exponent of 0.6 ± 0.1 . Finally, the entropy fit was determined to

be $(S - S_*) = 0.63 \ln(M/M_*) + 0.97$, which is consistent with inserting the density and temperature power-laws into the definition $S = \ln(T/\rho^{2/3})$. Hence, we indeed observe a high degree of self-similarity across M/M_* , despite not being a generally analytic prediction of the scale-free initial conditions.

We finish the scale-free evaluation by considering spherically averaged radial profiles of halos with fixed M/M_* at different redshifts. For this analysis, we focus on halos grouped into three mass bins: i) $2 \leq M/M_* \leq 4$, ii) $20 \leq M/M_* \leq 40$, and iii) $200 \leq M/M_* \leq 400$. From Eq. 65, these bins roughly correspond to halo masses of $M = 10^{12}$, 10^{13} , and $10^{14} h^{-1} M_\odot$, respectively, at redshift $z = 0$. For each halo, we calculate radial profiles of baryon density, temperature, and entropy along a common r/R_* axis. We then produce stacked measurements by computing mean profiles at each corresponding redshift, in addition to averaging across all redshifts, where we determine the standard deviation in quadrature.

The profile measurements are shown in Fig. 15. Similar to the integrated halo quantities, we find that the individual redshift results agree within their combined 1σ scatter for each mass bin. In the bottom panels, we highlight the scatter in the redshift measurements with respect to the combined stacked profile (over all redshifts) for the middle mass bin. We have chosen this bin as it displays the strongest test of self-similarity, containing five redshift samples spanning an order of magnitude in physical halo mass. In this case, we measure agreement at the 5% level for each fixed r/R_* bin, except in the outermost regions of the density and temperature

[†] Following from $T \propto M/R$, with $R \propto M^{1/3}$.

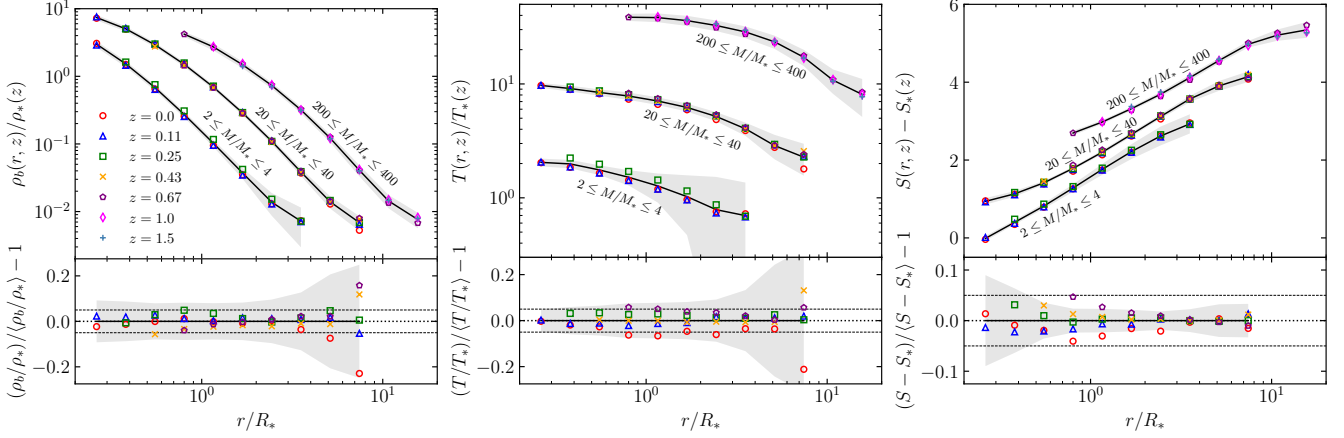


Figure 15. Stacked radial profiles of baryon density (left), temperature (center), and entropy (right) normalized to the non-linear scale (Eq. 65) for redshifts detailed in the legend. We show results for three separate M/M_* mass bins, which are separately labeled in each plot. The markers denote the mean stack for halos at a fixed redshift within a given mass bin, while the solid black line and gray shading trace the combined stack and its standard deviation. The bottom panels show the ratio with the combined stack profile of the middle mass bin, where the horizontal dashed lines indicate a $\pm 5\%$ spread.

profiles where the variance in the combined stack is also enhanced. We have calculated comparable results in the other two mass bins, indicating that radial self-similarity is achieved over three decades in M/M_* and nearly two decades in r/R_* .

As was done for the integrated quantities, we investigate potential self-similarity across mass bins, in this case by taking the three solid black curves in Fig. 15 and performing two operations. First, we use the fact that $R \propto M^{1/3}$ to shift the x -axis of each profile via $(r/R_*)(M/M_*)^{-1/3}$, where M is taken as the midpoint of each bin. Second, for the density and temperature profiles, we consider arbitrary scaling in the y -axis by $(Y/Y_*)(M/M_*)^\alpha$, where Y denotes either ρ_b or T and α is a free parameter. In the case of entropy, this is modified as a vertical translation, $(S - S_*) + \alpha \ln(M/M_*)$. We optimize for α by performing a uniform search to determine values that minimize the L1-norm between the three sets of curves. We find $\alpha = 0.03$, -0.63 , and -0.62 for ρ_b , T , and S , respectively. Fig. 16 shows the stacked radial profiles for the three M/M_* bins when scaled in this manner, where we observe a high degree of self-similarity in a mass range spanning two orders of magnitude at any fixed redshift. The optimized α values also match well with the fitting functions obtained in Fig. 14, which correspond to $\alpha = 0$, -0.63 , and -0.63 for ρ_b , T , and S , respectively.

In summary, we have found a high degree of temporal self-similarity for both integrated halo measurements and stacked radial profiles. Predicted scaling relations are obeyed at the 1%, 5%, and 2% level, for the global baryon density, temperature, and entropy, respectively, as well as at the $\sim 5\%$ level for the profiles of each quantity. Additionally, we have observed further similarity

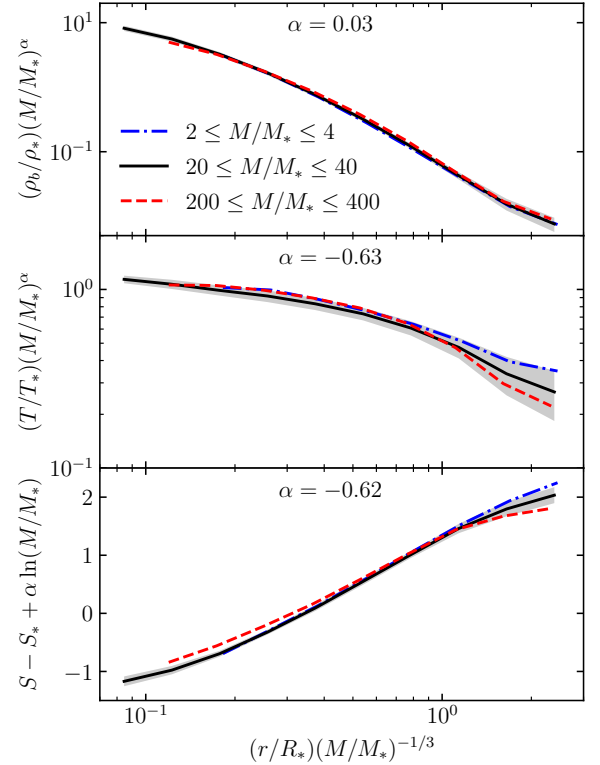


Figure 16. Stacked radial profiles showing baryon density (top), temperature (center), and entropy (bottom) for three M/M_* bins indicated in the legend. The radial profiles have been transformed in the x -axis by $(M/M_*)^{-1/3}$ and scaled in the y -axis using a procedure that minimizes the L1-norm between the three curves.

between halos of varying M/M_* , although the presence of this feature is not a general outcome of the scale-free derivation.

6. CONCLUSIONS AND FUTURE WORK

In this compendium we introduced the CRK-HACC framework, an enhancement of the highly performant cosmology code HACC to include the capability of modeling hydrodynamics. We summarized the primary software components that were developed for this extension (Section 3) as well as established solver correctness on a variety of standard validation tests in both the idealized fluid and cosmological domains (Section 4). Of particular note is the cluster comparison investigation (Section 4.2.3), where CRK-HACC displayed close agreement with other modern SPH and Eulerian-based solvers despite not including artificial conductivity in our methodology. We further analyzed scale-free simulations (Section 5), a useful exercise that can be repeated for cross-code validation, and has extensions that can incorporate radiative cooling models. As predicted by theory, the CRK-HACC solver demonstrates self-similarity of converged structure-forming quantities, such as integrated halo measurements and profiles.

The accuracy afforded by the CRKSPH approach combined with the performance of the HACC design will be important for properly including baryonic effects in upcoming large-volume cosmological simulations targeting survey predictions. CRK-HACC is optimized to exploit current and future supercomputing hardware, particularly GPU-accelerated systems. These capabilities will facilitate next-generation hydrodynamic simulations that encompass Gpc-scale volumes, providing excellent statistics of massive halos, and enabling numerous synthetic sky measurements.

While we have outlined the primary elements of the CRK-HACC framework in this paper, there are multiple components that warrant further explanation and examination. For example, our validation was limited to the adiabatic solver, neglecting the inclusion of subgrid sources and radiative effects. However, CRK-HACC has been furnished with a number of galaxy formation models (summarized in Section 3.7) that will be necessary to evolve baryonic processes important for structure formation. The complexities of formulating and calibrating subgrid models, particularly for cosmological probes, come with their own set of challenges and will be the focus of upcoming studies. Additionally, the incorporation and GPU-acceleration of the baryon-specific analysis pipelines (briefly discussed in Section 3.8) is interesting and useful in its own right, and will be the subject of study in a full performance analysis report.

There are further augmentations in CRK-HACC currently under development as well. These include neutrino extensions, as well as the capability to investi-

gate primordial non-Gaussianity effects. As discussed in Section 3.5, there are a number of intricacies involved with cosmological initial conditions (such as perturbation order and starting redshift), as well as additional considerations for multi-species and individual transfer functions. Circumstances are further complicated by the incorporation of massive neutrino cosmologies (e.g., Zennaro et al. 2017), where we intend to conduct comprehensive convergence investigations of these effects as well.

ACKNOWLEDGMENTS

We thank Mike Owen and Cody Raskin for their continued collaboration and guidance, as well as their contributions in both the origination and extensions of CRKSPH. SH acknowledges inspiring past discussions with Bryan (Bucky) Kashiwa in Los Alamos National Laboratory’s Theoretical Division. We recognize the efforts of HACC team members Hal Finkel, Patricia Larsen, Vitali Morozov, Adrian Pope, Esteban Rangel, and Tom Uram as well as helpful discussions and continuing collaboration with members of the Nyx team: Ann Almgren, Solène Chabanier, Zarija Lukić, Hannah Ross, and Jean Sexton.

Argonne National Laboratory’s work was supported under the U.S. Department of Energy contract DE-AC02-06CH11357. This research was supported by the Exascale Computing Project (17-SC-20-SC), a collaborative effort of the U.S. Department of Energy Office of Science and the National Nuclear Security Administration. This work used resources of the Oak Ridge Leadership Computing Facility, which is a DOE Office of Science User Facility supported under Contract DE-AC05-00OR22725. Additionally, this study utilized resources of the Argonne Leadership Computing Facility, which is a DOE Office of Science User Facility supported under Contract DE-AC02-06CH11357. This research also used resources of the National Energy Research Scientific Computing Center (NERSC), a U.S. Department of Energy Office of Science User Facility located at Lawrence Berkeley National Laboratory, operated under Contract No. DE-AC02-05CH11231 using NERSC award m3921 in 2021/22. CAFG was supported by NSF through grants AST-1715216, AST-2108230, and CAREER award AST-1652522; by NASA through grant 17-ATP17-0067; by STScI through grant HST-AR-16124.001-A; and by the Research Corporation for Science Advancement through a Cottrell Scholar Award. Lastly, NF would like to thank his mother for her contributions to the literacy of the paper; NF and co-authors hasten to add that no blame attaches to her for any remaining infelicities of language.

REFERENCES

- Agertz, O., Moore, B., Stadel, J., et al. 2007, *Monthly Notices of the Royal Astronomical Society*, 380, 963
- Almgren, A. S., Bell, J. B., Lijewski, M. J., Lukić, Z., & Van Andel, E. 2013, *The Astrophysical Journal*, 765, 39
- Angulo, R. E., & Hahn, O. 2021, arXiv preprint arXiv:2112.05165
- Angulo, R. E., Hahn, O., & Abel, T. 2013, *Monthly Notices of the Royal Astronomical Society*, 434, 1756
- Balsara, D. S. 1995, *Journal of Computational Physics*, 121, 357
- Barnes, J., & Hut, P. 1986, *nature*, 324, 446
- Bassett, B. R., & Owen, J. M. 2021, arXiv preprint arXiv:2104.07832
- Beck, A. M., Murante, G., Arth, A., et al. 2016, *Monthly Notices of the Royal Astronomical Society*, 455, 2110
- Benhaiem, D., Joyce, M., & Sylos Labini, F. 2017, *Monthly Notices of the Royal Astronomical Society*, 470, 4099
- Biffi, V., & Valdarnini, R. 2015, *Monthly Notices of the Royal Astronomical Society*, 446, 2802
- Binney, J., & Knebe, A. 2002, *MNRAS*, 333, 378
- Bird, S., Feng, Y., Pedersen, C., & Font-Ribera, A. 2020, *JCAP*, 2020, 002
- Blas, D., Lesgourgues, J., & Tram, T. 2011, *JCAP*, 2011, 034
- Bondi, H., & Hoyle, F. 1944, *Monthly Notices of the Royal Astronomical Society*, 104, 273
- Booth, C., & Schaye, J. 2009, *Monthly Notices of the Royal Astronomical Society*, 398, 53
- Bryan, G. L., Norman, M. L., Stone, J. M., Cen, R., & Ostriker, J. P. 1995, *Computer physics communications*, 89, 149
- Cabezón, R. M., Garcia-Senz, D., & Figueira, J. 2017, *Astronomy & Astrophysics*, 606, A78
- Chandrasekhar, S. 1961, *Hydrodynamic and Hydromagnetic Stability* (Oxford:Clarendon)
- Child, H. L., Habib, S., Heitmann, K., et al. 2018, *The Astrophysical Journal*, 859, 55
- Christensen, R. B. 1990, in *Nuclear Explosives Code Developers Conference*, Vol. UCRL-JC-105269, Lawrence Livermore National Lab (Lawrence Livermore Technical Report)
- Colombi, S., Bouchet, F., & Hernquist, L. 1995, arXiv preprint astro-ph/9508142
- Copeland, D., Taylor, A., & Hall, A. 2018, *Monthly Notices of the Royal Astronomical Society*, 480, 2247
- Cullen, L., & Dehnen, W. 2010, *MNRAS*, 408, 669
- Davis, M., Efstathiou, G., Frenk, C. S., & White, S. D. 1985, *The Astrophysical Journal*, 292, 371
- Dehnen, W., & Aly, H. 2012, *Monthly Notices of the Royal Astronomical Society*, 425, 1068
- Dilts, G. A. 1999, *International Journal for Numerical Methods in Engineering*, 44, 1115
- Duncan, M. J., Levison, H. F., & Lee, M. H. 1998, *The Astronomical Journal*, 116, 2067
- Durier, F., & Dalla Vecchia, C. 2011, *Monthly Notices of the Royal Astronomical Society*, 419, 465
- Efstathiou, G., & Eastwood, J. W. 1981, *MNRAS*, 194, 503
- Efstathiou, G., Fall, S. M., & Hogan, C. 1979, *Monthly Notices of the Royal Astronomical Society*, 189, 203
- Efstathiou, G., Frenk, C. S., White, S. D., & Davis, M. 1988, *Monthly Notices of the Royal Astronomical Society*, 235, 715
- Emberson, J. D., Frontiere, N., Habib, S., et al. 2019, *The Astrophysical Journal*, 877, 85
- Faucher-Giguère, C.-A. 2020, *Monthly Notices of the Royal Astronomical Society*, 493, 1614
- Forest, E., & Ruth, R. D. 1990, *Physica D: Nonlinear Phenomena*, 43, 105
- Frenk, C., White, S., Bode, P., et al. 1999, *The Astrophysical Journal*, 525, 554
- Frontiere, N., Raskin, C. D., & Owen, J. M. 2017, *Journal of Computational Physics*, 332, 160 [FRO17]
- Frontiere, N., Heitmann, K., Rangel, E., et al. 2021, arXiv preprint arXiv:2109.01956
- Gafton, E., & Rosswog, S. 2011, *Monthly Notices of the Royal Astronomical Society*, 418, 770
- Gingold, R. A., & Monaghan, J. J. 1977, *MNRAS*, 181, 375
- Haardt, F., & Madau, P. 2012, *The Astrophysical Journal*, 746, 125
- Habib, S., Pope, A., Finkel, H., et al. 2016, *New Astronomy*, 42, 49 [H16]
- Hahn, O., Rampf, C., & Uhlemann, C. 2021, *MNRAS*, 503, 426
- Hamming, R. W. 1998, *Digital filters* (Courier Corporation)
- Harnois-Déraps, J., van Waerbeke, L., Viola, M., & Heymans, C. 2015, *Monthly Notices of the Royal Astronomical Society*, 450, 1212
- Heitmann, K., Ricker, P. M., Warren, M. S., & Habib, S. 2005, *The Astrophysical Journal Supplement Series*, 160, 28
- Heitmann, K., White, M., Wagner, C., Habib, S., & Higdon, D. 2010, *The Astrophysical Journal*, 715, 104
- Heitmann, K., Frontiere, N., Rangel, E., et al. 2021, *The Astrophysical Journal Supplement Series*, 252, 19
- Hernquist, L., & Katz, N. 1989, *ApJS*, 70, 419
- Heß, S., & Springel, V. 2010, *Monthly Notices of the Royal Astronomical Society*, 406, 2289

- Hirschmann, M., Dolag, K., Saro, A., et al. 2014, *Monthly Notices of the Royal Astronomical Society*, 442, 2304
- Hockney, R. W., & Eastwood, J. W. 1988, *Computer simulation using particles* (crc Press)
- Hoffman, Y., & Ribak, E. 1991, *The Astrophysical Journal*, 380, L5
- Hopkins, P. F. 2012, *Monthly Notices of the Royal Astronomical Society*, 428, 2840
- . 2015, *Monthly Notices of the Royal Astronomical Society*, 450, 53
- Hopkins, P. F., Wetzel, A., Kereš, D., et al. 2018, *Monthly Notices of the Royal Astronomical Society*, 480, 800
- Hoyle, F., & Lyttleton, R. A. 1939, in *Mathematical Proceedings of the Cambridge Philosophical Society*, Vol. 35, Cambridge University Press, 405–415
- Hu, C.-Y., Naab, T., Walch, S., Moster, B. P., & Oser, L. 2014, *MNRAS*, 443, 1173
- Jain, B., & Bertschinger, E. 1998, *The Astrophysical Journal*, 509, 517
- Joyce, M., Garrison, L., & Eisenstein, D. 2021, *Monthly Notices of the Royal Astronomical Society*, 501, 5051
- Kaiser, N. 1986, *Monthly Notices of the Royal Astronomical Society*, 222, 323
- Klypin, A., Kravtsov, A. V., Bullock, J. S., & Primack, J. R. 2001, *The Astrophysical Journal*, 554, 903
- Komatsu, E., Smith, K. M., Dunkley, J., et al. 2011, *The Astrophysical Journal Supplement Series*, 192, 18
- Lacey, C., & Cole, S. 1993, *MNRAS*, 262, 627
- Lacey, C., & Cole, S. 1994, *Monthly Notices of the Royal Astronomical Society*, 271, 676
- Lebrun-Grandié, D., Prokopenko, A., Turcksin, B., & Slattey, S. R. 2020, *ACM Trans. Math. Softw.*, 47, doi:10.1145/3412558
- Lewis, A., Challinor, A., & Lasenby, A. 2000, *The Astrophysical Journal*, 538, 473
- L’Huillier, B., Park, C., & Kim, J. 2014, *New Astronomy*, 30, 79
- Liu, W. K., & Jun, S. 1998, *International Journal for Numerical Methods in Engineering*
- Liu, W. K., Jun, S., & Zhang, Y. F. 1995, *International Journal for Numerical Methods in Fluids*, 20, 1081
- Lucy, L. B. 1977, *AJ*, 82, 1013
- Ludlow, A. D., & Angulo, R. E. 2016, *Monthly Notices of the Royal Astronomical Society: Letters*, slw216
- Lukić, Z., Heitmann, K., Habib, S., Bashinsky, S., & Ricker, P. M. 2007, *The Astrophysical Journal*, 671, 1160
- Lukić, Z., Stark, C. W., Nugent, P., et al. 2014, *Monthly Notices of the Royal Astronomical Society*, 446, 3697
- McNally, C. P., Lyra, W., & Passy, J.-C. 2012, *The Astrophysical Journal Supplement Series*, 201, 18
- Mitchell, N., McCarthy, I., Bower, R., Theuns, T., & Crain, R. 2009, *Monthly Notices of the Royal Astronomical Society*, 395, 180
- Monaghan, J. J. 2005, *Reports on progress in physics*, 68, 1703
- Monaghan, J. J., & Gingold, R. A. 1983, *Journal of Computational Physics*, 52, 374 [MG83]
- Morris, J. P., & Monaghan, J. J. 1997, *Journal of Computational Physics*, 136, 41
- Naab, T., & Ostriker, J. P. 2017, *Annual review of astronomy and astrophysics*, 55, 59
- Navarro, J. F., Frenk, C. S., & White, S. D. M. 1997, *ApJ*, 490, 493
- Owen, J. M. 2014, *International Journal for Numerical Methods in Fluids*, 75, 749
- Owen, J. M., Weinberg, D. H., Evrard, A. E., Hernquist, L., & Katz, N. 1998a, *The Astrophysical Journal*, 503, 16
- Owen, J. M., Weinberg, D. H., & Villumsen, J. V. 1998b, *arXiv preprint astro-ph/9805097*
- Peebles, P. J. E. 1980, *The large-scale structure of the universe* (Princeton university press)
- Pelupessy, F. I., Jänes, J., & Zwart, S. P. 2012, *New Astronomy*, 17, 711
- Pillepich, A., Springel, V., Nelson, D., et al. 2018, *Monthly Notices of the Royal Astronomical Society*, 473, 4077
- Power, C., Read, J., & Hobbs, A. 2014, *Monthly Notices of the Royal Astronomical Society*, 440, 3243
- Power, C., Robotham, A. S. G., Obreschkow, D., Hobbs, A., & Lewis, G. F. 2016, *MNRAS*, 462, 474
- Prada, F., Klypin, A. A., Cuesta, A. J., Betancort-Rijo, J. E., & Primack, J. 2012, *Monthly Notices of the Royal Astronomical Society*, 423, 3018
- Price, D. J. 2008, *Journal of Computational Physics*, 227, 10040
- . 2012, *Journal of Computational Physics*, 231, 759
- Quinn, T., Katz, N., Stadel, J., & Lake, G. 1997, *arXiv preprint astro-ph/9710043*
- Raskin, C., & Owen, J. M. 2016, *ArXiv e-prints*: 1607.04293, *arXiv:1607.04293*
- Read, J. I., & Hayfield, T. 2012, *Monthly Notices of the Royal Astronomical Society*, 422, 3037
- Read, J. I., Hayfield, T., & Agertz, O. 2010, *Monthly Notices of the Royal Astronomical Society*, 405, 1513
- Rosswog, S. 2009, *New Astronomy Reviews*, 53, 78
- Rudd, D. H., Zentner, A. R., & Kravtsov, A. V. 2008, *The Astrophysical Journal*, 672, 19
- Saha, P., & Tremaine, S. 1992, *The Astronomical Journal*, 104, 1633
- Saitoh, T. R., & Makino, J. 2009, *The Astrophysical Journal Letters*, 697, L99

- . 2010, Publications of the Astronomical Society of Japan, 62, 301
- . 2016, The Astrophysical Journal, 823, 144
- Salmon, J. K., Moraes, M. A., Dror, R. O., & Shaw, D. E. 2011, in Proceedings of 2011 International Conference for High Performance Computing, Networking, Storage and Analysis, SC '11 (New York, NY, USA: Association for Computing Machinery)
- Schaye, J., Crain, R. A., Bower, R. G., et al. 2015, Monthly Notices of the Royal Astronomical Society, 446, 521
- Schoenberg, I. 1969, Journal of Approximation theory, 2, 167
- Sedov, L. I. 1946, Journal of Applied Mathematics and Mechanics, 10, 241
- Sembolini, F., Yepes, G., Pearce, F. R., et al. 2016, Monthly Notices of the Royal Astronomical Society, 457, 4063
- Shandarin, S. F., & Zeldovich, Y. B. 1989, Reviews of Modern Physics, 61, 185
- Sijacki, D., Springel, V., Di Matteo, T., & Hernquist, L. 2007, Monthly Notices of the Royal Astronomical Society, 380, 877
- Smith, R. E., Peacock, J. A., Jenkins, A., et al. 2003, Monthly Notices of the Royal Astronomical Society, 341, 1311
- Sod, G. A. 1978, J. Comput. Phys, 27, 1
- Springel, V. 2005, Monthly Notices of the Royal Astronomical Society, 364, 1105
- . 2010a, Monthly Notices of the Royal Astronomical Society, 401, 791
- . 2010b, Annual Review of Astronomy and Astrophysics, 48, 391
- Springel, V., Di Matteo, T., & Hernquist, L. 2005, Monthly Notices of the Royal Astronomical Society, 361, 776
- Springel, V., & Hernquist, L. 2003, Monthly Notices of the Royal Astronomical Society, 339, 289
- Springel, V., Pakmor, R., Zier, O., & Reinecke, M. 2021, Monthly Notices of the Royal Astronomical Society, 506, 2871
- Steinmetz, M., & Mueller, E. 1993, A&A, 268, 391
- Strang, G. 1968, SIAM journal on numerical analysis, 5, 506
- Taylor, G. I. 1950, Proceedings of the Royal Society of London. Series A. Mathematical and Physical Sciences, 201, 159
- Teyssier, R. 2002, Astronomy & Astrophysics, 385, 337
- Thacker, R., Tittley, E., Pearce, F., Couchman, H., & Thomas, P. 2000, Monthly Notices of the Royal Astronomical Society, 319, 619
- Toro, E. 1989, Proceedings of the Royal Society of London. A. Mathematical and Physical Sciences, 423, 401
- Townsend, R. 2009, The Astrophysical Journal Supplement Series, 181, 391
- Trac, H., & Pen, U.-L. 2004, New Astronomy, 9, 443
- Tuckerman, M., Berne, B. J., & Martyna, G. J. 1992, The Journal of chemical physics, 97, 1990
- Valkenburg, W., & Villaescusa-Navarro, F. 2017, Monthly Notices of the Royal Astronomical Society, 467, 4401
- van Daalen, M. P., Schaye, J., Booth, C., & Dalla Vecchia, C. 2011, Monthly Notices of the Royal Astronomical Society, 415, 3649
- van Leer, B. 1974, Journal of Computational Physics, 14, 361
- Vogelsberger, M., Marinacci, F., Torrey, P., & Puchwein, E. 2020, Nature Reviews Physics, 2, 42
- Vogelsberger, M., Nelson, D., Hernquist, L., et al. 2014, Monthly Notices of the Royal Astronomical Society, 444, 1518
- Wadsley, J., Veeravalli, G., & Couchman, H. 2008, Monthly Notices of the Royal Astronomical Society, 387, 427
- Wadsley, J. W., Keller, B. W., & Quinn, T. R. 2017, Monthly Notices of the Royal Astronomical Society, 471, 2357
- Weinberger, R., Springel, V., Hernquist, L., et al. 2016, Monthly Notices of the Royal Astronomical Society, 465, 3291
- Wendland, H. 1995, Advances in Computational Mathematics, 4, 389
- White, S. D. 1994, arXiv preprint astro-ph/9410043
- Widrow, L. M., Elahi, P. J., Thacker, R. J., Richardson, M., & Scannapieco, E. 2009, Monthly Notices of the Royal Astronomical Society, 397, 1275
- Wiersma, R. P., Schaye, J., Theuns, T., Dalla Vecchia, C., & Tornatore, L. 2009, Monthly Notices of the Royal Astronomical Society, 399, 574
- Yoshida, H. 1990, Physics letters A, 150, 262
- Zel'dovich, Y. B. 1970, Astronomy and Astrophysics, 5, 84
- Zennaro, M., Bel, J., Villaescusa-Navarro, F., et al. 2017, MNRAS, 466, 3244
- Zhu, Q. 2021, New Astronomy, 85, 101481